

# Lipid droplets and small extracellular vesicles: More than two independent entities

Géraldine C. Genard<sup>1</sup>  | Luca Tirinato<sup>1,2,3</sup>  | Francesca Pagliari<sup>1</sup> | Jessica Da Silva<sup>1</sup> | Alessandro Giammona<sup>4,5</sup> | Fatema Alquraish<sup>4</sup> | Maria Parra Reyes<sup>1</sup> | Marie Bordas<sup>6</sup> | Maria Grazia Marafioti<sup>1</sup> | Simone Di Franco<sup>7</sup> | Jeannette Janssen<sup>1</sup> | Daniel Garcia-Calderón<sup>1,8</sup> | Rachel Hanley<sup>1</sup> | Clelia Nistico<sup>1,9</sup> | Yoshinori Fukasawa<sup>10</sup> | Torsten Müller<sup>11,12</sup> | Jeroen Krijgsveld<sup>12,13</sup> | Matilde Todaro<sup>7</sup> | Francesco Saverio Costanzo<sup>9</sup> | Giorgio Stassi<sup>7</sup> | Michelle Nessling<sup>14</sup> | Karsten Richter<sup>14</sup> | Kendra K. Maass<sup>15</sup> | Carlo Liberale<sup>4</sup>  | Joao Seco<sup>1,8</sup>

<sup>1</sup>Division of Biomedical Physics in Radiation Oncology, German Cancer Research Center (DKFZ), Heidelberg, Germany

<sup>2</sup>Department of Experimental and Clinical Medicine, Nanotechnology Research Center, University of Magna Graecia, Catanzaro, Italy

<sup>3</sup>Department of Medical and Surgical Science, University Magna Graecia, Catanzaro, Italy

<sup>4</sup>Biological and Environmental Science and Engineering, King Abdullah University of Science and Technology (KAUST), Thuwal, Saudi Arabia

<sup>5</sup>Institute of Molecular Biomaging and Physiology (IBFM), National Research Council (CNR), Segrate, Italy

<sup>6</sup>Division of Molecular Genetics, German Cancer Research Center (DKFZ), Heidelberg, Germany

<sup>7</sup>Department of Health Promotion, Mother and Child Care, Internal Medicine and Medical Specialties (PROMISE), University of Palermo, Palermo, Italy

<sup>8</sup>Department of Physics and Astronomy, Heidelberg University, Heidelberg, Germany

<sup>9</sup>Department of Experimental and Clinical Medicine, University of Magna Graecia, Catanzaro, Italy

<sup>10</sup>Core Labs, King Abdullah University of Science and Technology, (KAUST), Thuwal, Saudi Arabia

<sup>11</sup>German Cancer Research Center, DKFZ, Heidelberg, Germany

<sup>12</sup>Medical Faculty, Heidelberg University, Heidelberg, Germany

<sup>13</sup>Proteomics of Stem Cells and Cancer, German Cancer Research Center, Heidelberg, Germany

<sup>14</sup>Electron Microscopy Facility, German Cancer Research Center (DKFZ), Heidelberg, Germany

<sup>15</sup>Hopp-Children's Cancer Center Heidelberg (KiTZ), Heidelberg, Germany

## Correspondence

Joao Seco, Division of Biomedical Physics in Radiation Oncology, German Cancer Research Center (DKFZ), Heidelberg, Germany.  
Email: [joao.seco@dkfz.de](mailto:joao.seco@dkfz.de)

Luca Tirinato, Department of Medical and Surgical Science, University Magna Graecia, 88100 Catanzaro, Italy.  
Email: [tirinato@unicz.it](mailto:tirinato@unicz.it)

## Abstract

Despite increasing knowledge about small extracellular vesicle (sEV) composition and functions in cell–cell communication, the mechanism behind their biogenesis remains unclear. Here, we reveal for the first time that sEV biogenesis and release into the microenvironment are tightly connected with another important organelle, Lipid Droplets (LDs). The correlation was observed in several human cancer cell lines as well as patient-derived colorectal cancer stem cells (CR-CSCs). Our results demonstrated that external stimuli such as radiation, pH, hypoxia or lipid-interfering drugs,

Géraldine C. Genard and Luca Tirinato contributed equally to the work.

This is an open access article under the terms of the [Creative Commons Attribution-NonCommercial](https://creativecommons.org/licenses/by-nc/4.0/) License, which permits use, distribution and reproduction in any medium, provided the original work is properly cited and is not used for commercial purposes.

© 2024 The Author(s). *Journal of Extracellular Biology* published by Wiley Periodicals LLC on behalf of International Society for Extracellular Vesicles.

Carlo Liberale, Biological and Environmental Science and Engineering, King Abdullah University of Science and Technology (KAUST), Saudi Arabia. Email: [carlo.liberale@kaust.edu.sa](mailto:carlo.liberale@kaust.edu.sa)

#### Funding information

Deutscher Akademischer Austauschdienst; HORIZON EUROPE Marie Skłodowska-Curie Actions, Grant/Award Number: 800924; King Abdullah University of Science and Technology, Grant/Award Number: OSR-CRG2018-3747; German-Israeli Helmholtz Research School in Cancer Biology—Cancer Transitional and Research Exchange Program, Grant/Award Number: Cancer-TRAX; Deutsche Krebshilfe, Grant/Award Numbers: 70115332, 70115445

known to affect the number of LDs/cell, similarly influenced sEV secretion. Importantly, through multiple omics data, at both mRNA and protein levels, we revealed RAB5C as a potential important molecular player behind this organelle connection. Altogether, the potential to fine-tune sEV biogenesis by targeting LDs could significantly impact the amount, cargos and properties of these sEVs, opening new clinical perspectives.

#### KEYWORDS

exosomes, hypoxia, iron metabolism, irradiation, lipid droplets, pH, Rab, small extracellular vesicles

## 1 | INTRODUCTION

In 2013 Professors James E. Rothman, Randy W. Schekman and Thomas C. Südhof were awarded with the Nobel Prize for their discoveries of machinery regulating vesicle traffic, a major transport system in human cells (Bonifacino, 2014). Their and other groups' works highlighted the importance of intra- and extracellular vesicles (EVs) in the cell–cell communication and their ability to modulate the cellular microenvironment.

Almost all mammalian cells produce EVs, defined as “lipid bilayer-enclosed extracellular structures” of different size and intracellular origin. EVs are characterised by their size, cell origin, molecular composition and functions (Mathieu et al., 2019). Small extracellular vesicles (sEVs) are distinguished from other EV subtypes by their small size (30–200 nm) and their ability to travel along the blood and lymph streams to reach distant organs from their sites of origin. Since they carry intracellular content of donor cells (including DNA, RNA, proteins and lipids), those sEVs influence the fate of acceptor cells (Jeppesen et al., 2019; Yáñez-Mó et al., 2015). Their roles have been described in many physiological and pathological conditions, such as cancer, cardiovascular disease, immune response and regeneration (Kalluri & LeBleu, 2020). In a tumour context, cancer cell-derived sEVs are believed to be secreted in large amount, with the ability to remodulate the tumour microenvironment and progression through various mechanisms, including immune evasion (Poggio et al., 2019), proliferation, invasion or metastasis (Kalluri & LeBleu, 2020).

sEVs have two different subcellular origins, either endosomal or non-endosomal, playing part in their heterogeneity. In particular, sEVs of endosomal origin, so-called *exosomes*, are nanoparticles released through the fusion of multivesicular bodies (MVBs) (containing intraluminal vesicles (ILVs)) with the plasma membrane (Mathieu et al., 2019).

Since all sEVs are shaped by phospholipids, we hypothesised that a shared lipid source generates their surrounding membrane, originating either from recycled plasma membrane through the endosomal pathway or from a novel phospholipid source.

For a long time, lipid droplets (LDs) were primarily identified as organelles for fat storage (Aboumrad et al., 1963). Currently, LDs are widely recognised as essential cellular hubs involved in numerous physiological and pathological processes, including cancer (Cruz et al., 2020; Tirinato et al., 2017). Nevertheless, many open questions about their formation, composition and role remain to be fully elucidated.

LDs are spherical organelles, which are found in the cytoplasm, and in some cases, in the nucleus of all eukaryotic cells (Sołtysik et al., 2019). They are characterised by a lipid-rich core (cholesterol esters (CEs) and triacylglycerols (TAGs)) surrounded by a phospholipid monolayer (Hashemi & Goodman, 2015). Although the LD-protein repertoire is cell-specific and influenced by the methodology used for their isolation, to date more than 150 specific LD-proteins have been detected in mammalian cells (Olzmann & Carvalho, 2019).

Besides their role in membrane biosynthesis, LDs are highly dynamic organelles, with their ongoing cycle of growth and consumption reflecting the cell's changing needs (Olzmann & Carvalho, 2019). In this regard, during cell expansion and division (which require membrane enlargement and increased biosynthesis of phospholipids), the fatty acids stored as TAGs in the LD core are mobilised either by lipolysis or by lipophagy (Olzmann & Carvalho, 2019). This allows the cell to sustain several metabolic processes and membrane biosynthesis.

In a tumour context, LDs are associated with numerous functions. For example, LD accumulation protects cells from oxidative stress damage by sequestering free fatty acid (Bailey et al., 2015). In the same context, increase in LD density is considered as a cancer stem cell marker in many tumours (Tirinato et al., 2015; Yue et al., 2014) and as a cell signature for radioresistance (Tirinato et al., 2021). Moreover, a role for LDs in the immune system modulation has also been reported in colorectal cancer (Cotte et al., 2018).

To their diverse functions, LDs must interact with other cellular components. They achieve this by establishing physical contact with various organelles, such as the endoplasmic reticulum (ER), peroxisomes, lysosomes, mitochondria and endosomes (Olzmann & Carvalho, 2019).

Several reports suggested a connection between the LDs and the intracellular vesicle formation (Liu et al., 2007; Olzmann & Carvalho, 2019). It has been demonstrated that adipose tissue is responsible for secreting the highest number of sEVs among all tissues, which is intriguing considering that the adipocytes also contain the largest amount of LDs (Thomou et al., 2017). It was also shown that these lipid-filled sEVs are then used by macrophages as a source of lipids (Flaherty et al., 2019).

Based on this evidence, we decided to explore the potential link between LDs and sEVs. For this purpose, we used various commercial human cancer cell lines (colon, lung, pancreatic and breast cancer cells) as well as patient-derived CR-CSCs. We analysed the impact of modulating cellular LD density on sEVs and the LD-sEV connection using multiple approaches, including different external stimuli (such as varying pH, oxygen concentration and ionising radiation), LD inhibitors and silencing of Ferritin Heavy Chain 1 (FTH1) due to its established role in LD formation (Tirinato et al., 2021).

## 2 | MATERIALS AND METHODS

### 2.1 | Cell cultures

Different human cancer cell lines, purchased from ATCC, were used in this study. Human colon adenocarcinoma cell lines HT-29 (HTB-38) and LoVo (CCL-229) were cultured in McCoy's 5A (Modified) Medium, GlutaMAX™ Supplement (1X) (Gibco-Thermo Fischer Scientific, USA; #36600-021) or Ham's F-12K (Kaighn's) Medium Nutrient Mix (1X) (Gibco-Thermo Fischer Scientific, USA; #21127-022) respectively. Human breast adenocarcinoma cell line MCF7 (HTB-22) was cultured in Dulbecco's Modified Eagle Medium (DMEM) high glucose (1X) (Gibco-Thermo Fischer Scientific, USA; #11995-065). Human non-small-cell lung carcinoma (NSCLC) cell line NCI-H460 (HTB-177) was cultured in Roswell Park Memorial Institute (RPMI) 1640 Medium (1X) (Gibco-Thermo Fischer Scientific, USA; #22400-089). Human pancreatic epithelioid carcinoma PANC01 (CRL-1469) cell line was cultured in RPMI 1640 Medium (1X) (Gibco-Thermo Fischer Scientific, USA; #22400-089). All media were supplemented with 10% (v/v) heat-inactivated foetal bovine serum (FBS) (Gibco-Thermo Fischer Scientific, USA; #10500-064). Cells were maintained in an incubator 5% CO<sub>2</sub> atmosphere at 37°C. Cells were split when a confluence of 90% was reached. All cell lines were routinely authenticated (Multiplex human Cell Authentication, DKFZ, Germany).

### 2.2 | Isolation of cancer stem cells from patients

CR-CSCs were isolated from patients affected by colorectal cancer (CRC) who underwent surgical resection, in accordance with ethical policy of the University of Palermo Committee on Human Experimentation. CR-CSC isolation and characterisation were carried out as reported elsewhere (Todaro et al., 2014).

Briefly, CRC samples, after being cut in small pieces, were grinded by surgical scissors at 37°C for 30 min in DMEM medium supplemented with 10 mg/mL of hyaluronidase (Sigma) and 0.6 mg/mL of collagenase (GIBCO). Cell pellets were, subsequently, cultured in a serum-free Ham's F-12 Nutrient Mix medium (Thermo Fisher Scientific) using ultra-low attachment cell culture flasks (Corning). CR-CSC samples #4, #8 and #21, growing as spheroids, were mechanically and enzymatically disaggregated by Accutase (Thermo Fisher Scientific), when reached 80% of confluency.

Short tandem repeat (STR) analysis using a multiplex PCR assay, including a set of 24 loci (GlobalFiler™ STR kit, Applied Biosystem, USA), was routinely used to authenticate CR-CSCs and compare them to the parental patient tissues.

### 2.3 | Cell culture and transduction

Lentiviral transduced MCF7 were stably transduced with a lentiviral DNA containing either an shRNA that targets the 196–210 region of the FTH1 mRNA (sh29432) (MCF-7shFTH1) or a control shRNA without significant homology to known human mRNAs (MCF-7shRNA). MCF-7 shRNA and MCF-7 shFTH1 were cultured in DMEM medium (Thermo Fisher Scientific) supplemented with FBS 10% (Thermo Fisher Scientific), puromycin 1 µg/mL (Sigma-Aldrich). Cells were maintained at 37°C in a humidified 5% CO<sub>2</sub> atmosphere.

### 2.4 | sEV-free FBS

Foetal bovine serum (FBS) (Gibco, Carlsbad, CA, USA) was ultra-centrifuged at 100,000 × g for 18 h at 4°C. FBS supernatant was then filtered through a 0.22 µm filter (Millipore, USA) and used for sEV-related experiments.

## 2.5 | Treatments (pH, irradiation, hypoxia, inhibitors)

To collect sEVs, H460 ( $1.8 \times 10^6$ ), MCF7 ( $1.0 \times 10^6$ ), PANC01 ( $1.5 \times 10^6$ ), HT29 ( $2.0 \times 10^6$ ) and LoVo ( $3.0 \times 10^6$ ) cells were seeded in their normal medium (penicillin/streptomycin free) in T75 cm<sup>2</sup> flasks (Greiner CELLSTAR) 24 h prior treatment.

In the case of LD staining, H460 ( $1.0 \times 10^5$ ), MCF7 ( $1.0 \times 10^5$ ), HT29 ( $1.0 \times 10^5$ ) and LoVo ( $1.0 \times 10^5$ ) cells were seeded onto 12 pre-autoclaved coverslips (Electron Microscopy Sciences, USA) in a 12-well cell culture plate (Greiner CELLSTAR) and cultured in their normal medium supplemented with 100 U/mL penicillin/streptomycin (Thermo Fischer Scientific, USA; #15140122). For x-ray irradiation (6 Gy),  $3.5 \times 10^5$  cells were seeded for both H460 and MCF7 cell lines whilst  $1.0 \times 10^5$  cells were seeded in control groups.

### 2.5.1 | pH treatment

24 h after seeding, H460 or MCF7 cells were divided in two groups: i) a control group, for which the medium was replaced with fresh adequate pH 7.4 medium; ii) a treated group, cultured with medium for which pH was adjusted to 6.5. The pH of both cell media was adjusted just prior the medium replacement to avoid any kind of pH variation due to oxidation. Treated cells were kept in culture for 72 h. Fresh medium was replaced every day for LD experiments.

To avoid the presence of exogenous sEVs in experiments intended to collect cancer cell-derived sEVs, cells were washed twice with Dulbecco's phosphate buffered saline (DPBS) (Sigma-Aldrich, USA; #8537) and sEV-free FBS media was used (penicillin/streptomycin free).

### 2.5.2 | Irradiation treatment

24 h after seeding, samples with H460 or MCF7 cells were divided in two groups: i) a control group, unirradiated and ii) a treated group, irradiated with 6 Gy x-rays using a MultiRad 225 kV (Faxitron, Germany) irradiator. Treated cells were kept in culture for 72 h to select only radioresistant cells at the end of the incubation time. Fresh medium was replaced every day for LD experiments. For PANC01 and H460 cells, 2, 4, 6 or 8 Gy were also used.

As for pH treatment, cells were washed with DPBS, and media were supplemented with sEV-free FBS (penicillin/streptomycin free).

### 2.5.3 | Hypoxia culturing conditions

All experiments in hypoxic conditions were conducted by culturing CR-CSCs in a three-gas incubator (Thermo Fisher) at 37°C with a 2% of Oxygen and with 5% CO<sub>2</sub> atmosphere for 72 h. LD staining and RNA-seq have been carried at the end of the incubation time keeping all samples in hypoxic conditions.

### 2.5.4 | Lipid droplet inhibition

Two different LD inhibitors were here tested: PF-06424439 (a diacylglycerol acyltransferase 2 (DGAT2) inhibitor; Saint Louis, MO, USA, CN-PZ0233) and Triacsin C (a long-chain fatty acyl CoA synthetase inhibitor) (Cayman Chemical, #10007448).

Both treatments were carried out for 72 h with 30 μM of PF-06424439 or 7.5 or 10 μM of Triacsin C. Drug solutions were prepared freshly for every replicates. As for other treatments, cells were washed with DPBS and media was supplemented with sEV-free FBS (penicillin/streptomycin free).

### 2.5.5 | Transfection with siRNA

HT29 cells were either seeded in 12-well plates ( $1.0 \times 10^5$  cells/ well) or in T75 flask ( $1.5 \times 10^6$  cells) 24 h prior transfection. The next day, cells were transfected with a unique 27mer siRNA duplex targeting RAB18 (Origene, #SR307888), RAB5C (Origene, #SR303957) or RAB7A (Origene, #SR305302), using siTran 2.0 siRNA transfection reagent (Origene, #TT320001). Three different sequences per each target were used separately, written as #1, #2 and #3. The day of transfection, siRNAs were mixed together with the transfection reagent (1X) to a final concentration of 10 nM for 15 min. The solution was thereafter added to the cells drop-wise and the cells were incubated for 72 h until ulterior analyses were performed.

## 2.6 | FACS sorting

HT29 cells were detached with TrypLE™ Express (Gibco, USA, #12604013) and then centrifuged for 5 min at  $300 \times g$ . Cells were thereafter stained with LD540 for 10 min at  $37^\circ\text{C}$  in the dark. Both samples were washed with DPBS three times to remove the excess of the dye and then resuspended in the sorting buffer (PBS Ca/Mg-free, BSA 0.5%, EDTA 2 mM and Hepes 15 mM).

Two populations were then sorted based on the LD abundance using a FACSAria Fusion Cell sorter (BD Bioscience).

The 10% LD<sup>High</sup> (most bright) and 10% LD<sup>Low</sup> (most dim) cells were collected and, soon after were seeded on a coverslip using a cytospin centrifuge (Thermo Shandon Cytospin3, Marshall Scientific, USA). Cells were then fixed with 4% PFA and an anti-CD63 (NOVUS #NBP2-52225, Germany) was used at a 1/1000 dilution in PBS+BSA 1% for 2 h. Thereafter, a donkey anti-mouse IgG (H+L) Alexa Fluor 647 (Thermo Fisher #A-31571, USA), used at 1/2000 dilution in PBS+BSA 1% for 1 h allowed us to stain the MVBs within the cells. Finally, cells were stained with 1 mg/mL Hoechst 33342 (Thermo Fisher Scientific, CN-H3570) for 20 min before being processed for the optical imaging acquisition.

## 2.7 | Immunofluorescence and confocal microscopy

### 2.7.1 | Lipid droplet staining

LD variation among the different treatments was assessed by staining the investigated cell samples with two different dyes, depending on the experiment needs: LD540 and Bodipy 493/503 (Thermo Fisher, CN-D2191). Briefly, cells were seeded onto a coverslip and left in culture the time necessary for the experiment endpoints (72 h for irradiation, hypoxia and LD inhibition, whilst only 24 h for pH). When ready, cells were washed with DPBS, fixed with 4% PFA and then stained with 0.1 mg/mL LD540 or 2 mM Bodipy, both in DPBS. The volumes of the staining solutions were kept constants for all the analysed cell samples. Nuclei were stained with 1 mg/mL Hoechst 33342 (Thermo Fisher Scientific, CN-H3570).

### 2.7.2 | CD63 and Alix plasmid transfection for confocal microscopy

Plasmids mCherry-hAlix (plasmid#21504) and pCMV-Sport6-CD63-pHluorin (plasmid #130902) were purchased from Addgene. Cells were plated at a density of  $7.5 \times 10^4$  onto glass coverslips in 12-well plates and allowed to grow in the incubator for 24 h. Then the cells were irradiated (8 Gy) and were immediately transfected with the plasmids encoding CD63 or Alix, using FuGENE HD reagent (Promega, E2311, USA) with a FuGENE HD:DNA ratio of 4:1. After 48 h post transfection the cells were washed with DPBS, fixed with 4% PFA for 10 min and then stained with 1 mg/mL Hoechst 33342. The images were taken exactly as mentioned in the above paragraph. For sorted HT29 LD<sup>Low</sup> and HT29 LD<sup>High</sup>, as well as MCF7 shRNA and shFTH1, CD63 antibody (1:1000, Novus #NBP2-42225) and a goat anti-mouse IgG AlexaFluor 647 (ThermoFisher A-21235) were used to stain the CD63<sup>+</sup> MVBs.

### 2.7.3 | LysoTracker staining

After sorting, cells were centrifuged at 1200 rpm for 5 min, counted and  $5 \times 10^5$  cells were seeded onto coverslips using Cytospin®. The coverslip were washed with PBS and stained with LysoTracker™ Red DND-99 (MolecularProbes, ThermoFisher Scientific) for 45 min at  $37^\circ\text{C}$ . Thereafter, the cells were washed thrice and stained with 1 mg/mL Hoechst 33342. Finally, cells were fixed for 15 min in 4% of paraformaldehyde at room temperature. Samples were washed thrice, coverslips were mounted onto a glass slide and sealed with nail polish. After acquisition, ImageJ was used to quantify the LysoTracker area per cell.

### 2.7.4 | Confocal microscopy

Whole z-stacks images for the stained cells were taken by using a Zeiss LSM710 or Leica SP5 confocal microscope systems equipped with a 40× (lipid droplets) or 63× (multivesicular bodies, MVBs) oil immersion i-Plan Apochromat (numerical aperture 1.40) objectives. LD540 and Bodipy 493/503 were visualised using the 488 nm laser excitation and a 505–530 nm band-pass filter.

## 2.8 | Lipid droplet staining for flow cytometry analysis

Briefly,  $1.5 \times 10^6$  cells were seeded into T75 cm<sup>2</sup> flasks (Greiner CELLSTAR) 24 h prior irradiation (2, 4, 6, 8 and 10 Gy) and left in culture for 72 h after irradiation. Cells were detached with TrypLE™ Express (Gibco, USA, #12604013) and then centrifuged for 5 min at  $300 \times g$ . Cells were thereafter stained with 0.1 mg/mL LD540 for 10 min at  $37^\circ\text{C}$  in the dark. Samples were washed with DPBS three times in order to remove the excess of the dye and then resuspended in the sorting buffer (PBS Ca/Mg-free, BSA



0.5%, EDTA 2 mM and Hepes 15 mM). PI (Sigma-Aldrich, #P4864, Germany) was used to stain dead cells. Finally, the samples were analysed using a FACS Canto II (BD Biosciences, USA).

## 2.9 | Differential centrifugation and sEV isolation by size exclusion chromatography

Collected supernatants were supplemented with 1 mM Phenylmethylsulfonyl Fluoride (PMSF—Serva, Germany; #32395) and 100 U/mL penicillin/streptomycin (Thermo Fischer Scientific, USA; #15140122) before being centrifuged at  $300 \times g$  for 10 min at  $4^\circ\text{C}$  in a swing-out centrifuge to remove cellular debris. Resulting  $2000 \times g$  supernatants were transferred into ultracentrifugation tubes (Thin-wall, Polyallomer 38.5 mL tubes, Beckman Coulter, USA; #326823) and centrifuged at  $100,000 \times g$  for 2 h at  $4^\circ\text{C}$  using a Beckman L8-55MV ultracentrifuge (Beckman Coulter GmbH, Krefeld, Germany) with a SW27 Swinging-Bucket Rotor. Resulting  $100,000 \times g$  pellets were resuspended in 200  $\mu\text{L}$  of 0.22- $\mu\text{m}$ -filtered PBS. Size exclusion chromatography was then used to separate the sEVs from the contaminants (e.g., proteins), as previously reported (Bordas et al., 2020).

Briefly, single qEV 35 nm columns (Izon, Christchurch, New Zealand) were allowed to reach room temperature for 30 min. The resuspended pellet fraction (200  $\mu\text{L}$ ) was added onto the column. As soon as the sample volume was taken up by the column, 0.22  $\mu\text{m}$ -filtered PBS was added to the top of the column tube. The following fractions were collected: F0 (800  $\mu\text{L}$  = void volume of the column) and F1 to F7 (200  $\mu\text{L}$  each), according to the manufacturer's instructions.

## 2.10 | Protein extraction and quantification (Cells and sEVs)

### 2.10.1 | Bicinchoninic acid

Protein concentration of cell samples was assessed employing Pierce™ BCA Protein Assay Kit (Thermo Fisher Scientific Inc., Waltham, MA, USA). Cells were lysed in 300  $\mu\text{L}$  of 1 $\times$  RIPA buffer (Abcam, Cambridge, UK) supplemented with Halt™ Protease Inhibitor Cocktail, EDTA-free (100X) (Thermo Fisher, USA; #78425) and Halt™ Phosphatase Inhibitor Cocktail, (100X) (Thermo Fisher, USA, #78428). Samples were incubated for 20 min on ice and then centrifuged at  $17,000 \times g$  for 20 min at  $4^\circ\text{C}$ . Resulting supernatants were subjected to BCA assay according to the manufacturer's instructions. Absorbance was assessed at 562 nm with the use of a plate reader.

### 2.10.2 | Qubit

To determine the protein concentration of the isolated sEV samples, Qubit Protein Assay Kit (Life Technologies, USA) was used. SDS (Thermo Fisher Scientific, DE) was used to extract proteins. Briefly, 0.8  $\mu\text{L}$  SDS 2% and 7.2  $\mu\text{L}$  sEV sample were added in labelled Qubit assay tubes and vortexed for 30 s. The resulting samples were then processed according to the manufacturer's instructions. For the standards (Qubit™ protein standard #1, #2, #3), 0.8  $\mu\text{L}$  SDS 2% and 10  $\mu\text{L}$  standards were added to the corresponding labelled Qubit tubes.

## 2.11 | Nanoparticle tracking analysis (NTA)

Particle quantification of sEV samples was performed via NTA using NanoSight LM10 equipped with a 405 nm laser (Malvern Instruments, Malvern, UK). For the NTA analysis, samples were diluted 1:250 in 0.22  $\mu\text{m}$ -filtered PBS. Camera level and detection threshold were set up at 13 and 1.8, respectively. The absence of background was verified using 0.2  $\mu\text{m}$ -filtered PBS. For each sample, five videos of 40 s each were recorded and analysed using the NTA 3.0 software version (Malvern Instruments, Malvern, UK).

## 2.12 | Immunoblotting

sEVs were lysed in RIPA Lysis and Extraction Buffer 10X (Cell Signalling Technology, USA #98010) for 20 min on ice. Per lane, 19.5  $\mu\text{L}$  of protein samples were loaded onto 10% polyacrylamide gels. Following SDS-PAGE and protein transfer, membranes were blocked in 5% bovine serum albumin in PBS-Tween 0.1%, and primary antibodies against CD63 (1:1000, Novus #NBP2-42225), CD81 (1:1000, ProSci Inc., San Diego, CA, USA, #5195), CD9 (1:1000, Cell Signalling Technology, Danvers, MA, USA, #13174) and HSC-70 (1:1000 Santa Cruz #C-7298) were used to detect sEV markers.

Calnexin (1:500, GeneScript, Piscataway, NJ, USA, #A0124040), Cytochrome C (1:750, GeneScript, Piscataway, NJ, USA, #A0150740), GM130 (1:1000, Cell Signalling Technology, Danvers, MA, USA, #12480), Enolase 1 (ENO-1) (1:1000, Abgent, San

Diego, CA, #AP6526c), RAB18 (ProteinTech # 11304-1-AP), RAB5C (Novus, #NBPI-80858) and RAB7A (Novus, #NBPI-87174) were used in indicated dilutions in 5% BSA in PBS-Tween 0.1% when cell proteins were compared to sEV ones, in order to exclude possible contaminants in sEV fractions.

Either HRP-linked Goat anti-Rabbit (Cell Signalling, USA; #7074), HRP-linked Goat anti-Mouse (Cell Signalling, USA; #7076) or HRP-linked Goat anti-Mouse (Thermo Fisher Scientific, USA; #631462) were used as secondary antibodies. Signals were visualised after secondary antibody hybridisation by chemiluminescence detection reagent (Bio-Rad Lab, Hercules, CA, USA, #1705061) with Amersham Imager 680 (GE Healthcare, USA).

## 2.13 | Electron microscopy (EM)

For negatives staining EM, sEV fractions (F2) were adsorbed onto pure carbon-coated EM-grids for 5 min, washed in aqua bidest and negatively stained with 1% aqueous uranyl acetate. For immuno-EM, sEV fractions were adsorbed on formvar-carbon-coated EM-grids. The incubation with primary antibody (anti-CD63, 1:1000, BD Pharmingen, USA, #556019) was performed after buffer wash and incubation with blocking agent (Aurion, Wageningen, The Netherlands). Protein A-Au was used as reporter (CMC, UMC Utrecht, The Netherlands, size of Au-grains 10 nm). Micrographs were taken with a Zeiss EM 910 or EM 912 at 80 kV (Carl Zeiss, Oberkochen, Germany) using a slow scan CCD camera (TRS, Moorenweis, Germany).

## 2.14 | RNA sequencing analysis

Total RNA was extracted by RNeasy Mini Kit (Qiagen) and mRNA libraries were prepared using TruSeq® Stranded mRNA Library Prep. Next-Generation Sequencing (NGS) technology (RNA-seq) was used to identify some vital biological processes and pathways involved in fatty acid modulation on CSCs cultured in Hypoxia and Normoxia. Illumina HiSeq 4000 and NovaSeq 6000 were used to perform transcriptome sequencing. The reads were aligned to GRCh38/hg38 of the human genome using STAR version 2.6.1d. Alignments were validated using a combination of FastQC version 0.11.8, SAMtools version 1.9 and MultiQC version 1.7 (Ewels et al., 2016; Li et al., 2009). Transcript abundance estimation was further performed using Salmon version 0.14.1 followed by importing them at the gene level with tximport version 1.14.0 (Patro et al., 2017; Sonesson et al., 2015). Subsequently, expression analysis at the gene level was conducted with DESeq2 version 1.26.0 (Love et al., 2014). Targeted gene analysis of commonly known genes and MORPHEUS Versatile matrix visualisation and analysis software were used to visualise the datasets as heat maps (Morpheus, <https://software.broadinstitute.org/morpheus>).

## 2.15 | Proteomic analyses

### 2.15.1 | Cells

MCF7-shRNA and MCF7-shFTH1 cells were washed twice and then scraped into 2 mL of cold PBS. Cells were then centrifuged at  $300 \times g$  for 5 min. Each pellet was incubated with 1 mL of 1X Ripa Buffer (Cell Signalling) added with Halt™ Protease Inhibitor Single-Use Cocktail, (Thermo Fisher Scientific) and Halt™ Phosphatase Inhibitor Single Use Cocktail (Thermo Fisher Scientific), both diluted 1:100 for 10 min on ice. Lysates were then sonicated (40% amplitude, 10 s/cycle; 3 cycle; 4°C) and incubated for 15 min on ice. 100 mL of Benzonase 2,75 U/mL (Millipore-Novagen) was added to lysates, incubated in ice for 10 min and then centrifuged at  $2500 \times g$  for 30 min at 4°C. The supernatants were collected. Protein concentration was measured by BCA Protein assay kit (Thermo Fisher Scientific) at 562 nm.

### 2.15.2 | sEVs

The protein quantification was performed with Qubit assay as described in section 10 (protein quantification).

### 2.15.3 | Sample processing

Samples were thawed and extensively vortexed before proceeding. Subsequently, for each sample, 10 µg protein were processed in a 1 µg/ 3 µL concentration in 1% SDS and 100 mM ammonium bicarbonate (ABC, Sigma-Aldrich). In brief, 10 mM TCEP, 40 mM chloroacetamide (CAA), 100 mM ABC and 1X protease inhibitor cocktail (PIC, cOmplete, Sigma-Aldrich) were added to each sample, followed by incubation at 95°C for 5 min. Protein binding to Sera-Mag Speed Beads (Fisher Scientific, Germany)

**TABLE 1** List of the primers used for the RT-PCR gene analysis.

Gene	Primer forward 5'→3'	Primer reverse 5'→3'	NCBI reference sequence
<i>HPRT1</i>	TTGACACTGGCAAAACAATG	GTCCTTTTCACCAGCAAGC	NM_000194.3
<i>STEAP3</i>	GAGGTCATCTTTGTGGCTGTG	CTCTTGCTCTGTAGGGTTGCT	NM_182915.3
<i>TFRC</i>	CTGGTAAACTGGTCCATGCT	GTGATTTTCCCTGCTCTGAC	NM_003234.4
<i>ANXA1</i>	GACCGATCTGAGGACTTTGG	CTCTGCGAAGTTGTGGATAG	NM_000700.3
<i>STX7</i>	GAAGGATCGCTTAGTGGCAG	CACTCTGGAAGTGGCTCTTAC	NM_001326578.2

was induced by increasing the buffer composition to 50% acetonitrile (ACN, Pierce—Thermo Scientific). The bead stock was prepared as follows: 20  $\mu$ L of Sera-Mag Speed Beads A and 20  $\mu$ L of Sera-Mag Speed Beads B were combined and rinsed with  $1 \times 160 \mu$ L ddH<sub>2</sub>O,  $2 \times$  with 200  $\mu$ L ddH<sub>2</sub>O and re-suspended in 20  $\mu$ L ddH<sub>2</sub>O for a final working stock of which 2  $\mu$ L were added per sample. The autoSP3 protein clean-up was performed with  $2 \times$  ethanol (EtOH, VWR International GmbH, Germany) and  $2 \times$  ACN washes. Reduced and alkylated proteins were digested on-beads and overnight at 37°C in a lid-heated PCR cycler (CHB-T2-D ThermoQ, Hangzhou BIOER Technologies, China) in 100 mM ABC with sequencing-grade modified trypsin (Promega, USA). Upon overnight protein digestion, each sample was acidified to a final concentration of 1% trifluoroacetic acid (TFA, Biosolve Chimie). MS injection-ready samples were stored at  $-20^\circ\text{C}$ .

## 2.15.4 | Data acquisition and processing

For the data acquisition a timsTOF Pro mass spectrometer (Bruker Daltonics) was equipped with an Easy nLC 1200 system (Thermo). An equivalent of 200 ng protein per sample was injected using the following method: peptides were separated using the Easy nLC 1200 system fitted with an analytical column (Aurora Series Emitter Column with CSI fitting, C18, 1.6  $\mu$ m, 75  $\mu$ m  $\times$  25 cm) (Ion Optics). The outlet of the analytical column with a captive spray fitting was directly coupled to a timsTOF Pro (Bruker) mass spectrometer using a captive spray source. Solvent A was ddH<sub>2</sub>O (Biosolve Chimie), 0.1% (v/v) FA (Biosolve Chimie), and solvent B was 100% ACN in dH<sub>2</sub>O, 0.1% (v/v) FA. The samples were loaded at a constant pressure of 800 bar. Peptides were eluted via the analytical column at a constant flow of 0.4  $\mu$ L per minute at 50°C. During the elution, the percentage of solvent B was increased in a linear fashion from 2% to 17% in 22.5 min, then from 17% to 25% in 11.25 min, then from 25% to 37% in 3.75 min and from 37% to 80% in a further 3.75 min. Finally, the gradient was finished with 3.75 min at 80% solvent B. Peptides were introduced into the mass spectrometer via the standard Bruker captive spray source at default settings. The glass capillary was operated at 1600 V and 3 L/min dry gas at 180°C. Full scan MS spectra with mass range  $m/z$  100 to 1700 and a  $1/k_0$  range from 0.85 to 1.3  $\text{V}^*\text{s}/\text{cm}^2$  with 100 ms ramp time were acquired with a rolling average switched on (10 $\times$ ). The duty cycle was locked at 100%, the ion polarity was set to positive, and the TIMS mode was enabled. The active exclusion window was set to 0.015  $m/z$ ,  $1/k_0$  0.015  $\text{V}^*\text{s}/\text{cm}^2$ . The isolation width was set to mass 700–800  $m/z$ , width 2–3  $m/z$  and the collision energy to  $1/k_0$  0.85–1.3  $\text{V}^*\text{s}/\text{cm}^2$ , energy 27–45 eV.

The resulting raw files were searched using MaxQuant version 2.0.3.0 using the default settings unless otherwise stated. Label-free quantification (LFQ) and intensity-based absolute quantification (iBAQ) were applied using the default settings. Matching between runs was enabled. The resulting proteinGroups and peptide tables were further analysed using matrixQCvis and R.

Protein analysis of commonly known proteins was performed using STRING (<https://string-db.org>; v.11.5) and cytoscape (v. 3.9.1).

## 2.16 | Real time-polymerase chain reaction (RT-qPCR)

Total RNA extraction, cDNA synthesis and qPCR were performed according to a procedure described elsewhere (Tirinato et al., 2021; Nisticò et al., 2021). The list of primers used is presented below (Table 1).

## 2.17 | Statistical analysis

### 2.17.1 | Image analysis

Twelve-bit z-stack images were acquired and post-processed for the LD quantification as reported elsewhere (Tirinato et al., 2021). Briefly, the background was subtracted from all images using ImageJ's Rolling ball radius tool. After that, all images were



processed with Gaussian filter, thresholded and segmented with Find Maxima tool. At this point, processed images were analysed with Analyse Particle tools. The whole image processing was set up automatically thanks to the in-house developed Fiji macro generously provided by Dr. Damir Krunic. Statistical analysis was performed by Student's *t*-test with unequal variances. Only *p*-values below 0.05 were considered statistically significant between two groups.

### 2.17.2 | sEVs

Results of the functional analysis were analysed for statistical significance with GraphPad PRISM 8.0 software (GraphPad Software, San Diego, CA, USA), using unpaired *t*-test or one-way analysis of variance (ANOVA), followed by Tukey's multiple comparisons. The differences between means were considered significant if  $p \leq 0.05$ . The results are expressed as the means  $\pm$  standard deviation.

## 3 | RESULTS

### 3.1 | The number of LDs strongly correlates with the release of sEVs in colorectal cancer cell lines

To evaluate if there was a possible connection between cellular LD count and sEV release, we first compared both the number of LDs and the average amount of released sEVs per cell, in two different colorectal cancer cell lines, LoVo and HT29 (**Figure 1**). As shown by z-stack projections of confocal microscopy images and by the associated quantification, HT29 contained significantly more LDs per cell than LoVo 72 h after seeding (**Figure 1a**). In parallel, the released sEVs were studied for both cell lines at the same time point. The sEV isolation protocol, based on the combination of differential centrifugation steps and size exclusion chromatography (SEC), was used as described in the Material & Methods (section 9) (Bordas et al., 2020) and pictured in **Figure S1A**. The purity of the sEV samples was validated by checking the presence of exosomal markers (CD63, CD81 and CD9) as well as the absence of Golgi (GM130), endoplasmic reticulum (Calnexin), mitochondrial (Cytochrome C) and plasma membrane and cytoplasmic (Enolase 1, HSC-70) markers in the sEV preparations and compared to cell lysate (**Figure S1B**). The EM analysis of the sEV preparations showed the characteristic donut-shaped morphology of sEVs obtained with TEM and a size ranging around 100 nm (**Figure 1b**). Similarly, we could determine the number of particles and their size by using Nanoparticle Tracking Analysis (NTA). The average size of particles peaked at 148 nm for LoVo cells and 133 nm for HT29 cells (**Figure S1C**). The NTA measurement (**Figure 1c**) and the protein quantification (**Figure S1D and S1E**) also confirmed a higher amount of sEVs released per cell for HT29 as compared to LoVo cells. We next aimed to identify exosomal markers by Western Blotting to confirm the higher number of sEVs released by HT29 cell line. By loading the same volume of each sample, we observed that exosomal markers (CD9, CD63, CD81 and HSC-70) were significantly more expressed in the sEV fractions collected from HT29 than LoVo cell line (**Figure 1d**). In accordance with the literature (De Maio, 2011), we found the presence of HSC-70 both in the cellular and sEV fractions, with a predominance for the cellular fraction. Whilst the EV number fold change between LoVo cells and HT29 cells was around 3-fold, the expression of some cargo proteins (CD63, CD81, CD9 and HSC-70) ranged from 2-fold to 14-fold. It is quite common to observe qualitative (presence or absence of proteins) and quantitative (protein abundance) differences in cargo among sEV samples across technical and biological replicates. This might be explained by the different sensibility between NTA and western blot. Finally, since the number of LDs may vary within the same cell line, we sorted HT29 cells based on their cellular LD count.

To confirm the effectiveness of the sorting, the number of LDs was evaluated by confocal microscopy (**Figure S1F**). Concurrently, multivesicular bodies (MVBs) were assessed by confocal microscopy as well. The images indicated a high CD63<sup>+</sup>MVB numbers for the HT29 LD<sup>High</sup> fraction in comparison to the HT29 LD<sup>Low</sup> counterpart (**Figure 1e**). As the staining for CD63 required a permeabilisation, and therefore lipid digestion, it was not possible to assess both LDs and CD<sup>+</sup>MVBs on the same micrographs. This difference was also evaluated by Western Blot on the cellular protein content. These results confirmed a higher expression of CD63 in HT29 LD<sup>High</sup> as compared to HT29 LD<sup>Low</sup> cells (**Figure S2A**).

These findings collectively indicate that the intracellular LD count follows a similar trend to that of released sEVs.

### 3.2 | Inhibition of LD metabolism reduces sEV release

Thereafter, we decided to target LD biosynthesis in HT29 cells by using two lipid inhibitors affecting two different steps of the LD biogenesis (**Figure 2a**).

The first drug acts as an inhibitor of long fatty acetyl-CoA synthetases (Triacsin-C), whilst the second one blocks the glycerolipid synthesis (PF-06424439). Triacsin-C and PF-06424439 were used at a concentration of 10 and 30  $\mu$ M, respectively. The choice of the inhibitor concentrations was made based on the literature for Triacsin-C (Cotte et al., 2018) and on the evaluation

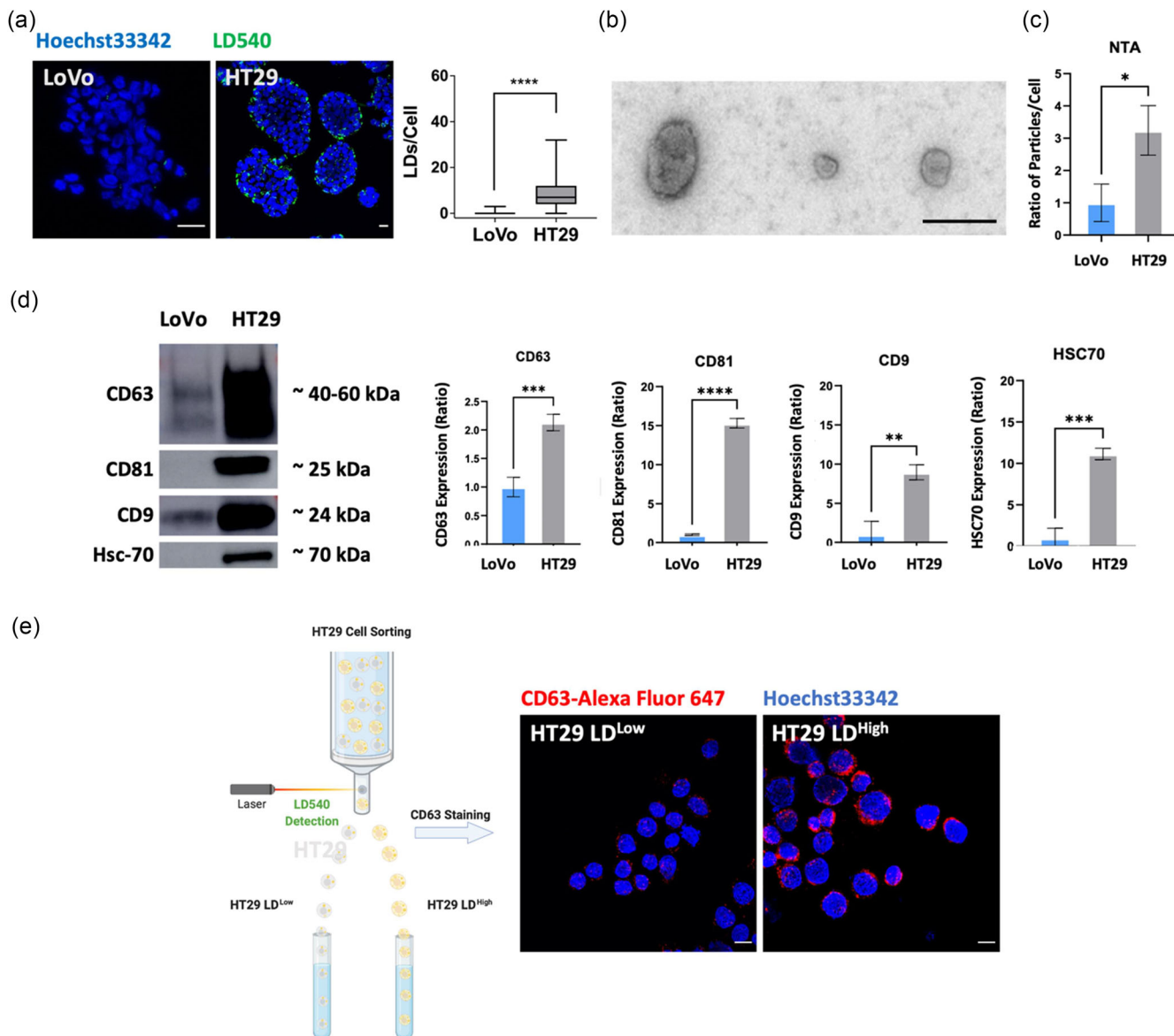


**FIGURE 1** Analysis of cellular LD count and sEV release in LoVo and HT29 colorectal cancer cell lines. (a) HT29 and LoVo cell lines were stained with LD540 (green) for LDs and DAPI (blue) for nuclei and imaged with a confocal microscope provided with a 100X objective (Leica Microsystems; Concord, Ontario, Canada). The pinhole was set for a slice thickness of 17.4  $\mu$ m, with an interval between slices of 0.9  $\mu$ m. Z-projection of the z-stack acquisitions is shown (left). Displayed are the merged images of the LD540 and DAPI staining from one independent experiment (Scale bar, 20  $\mu$ m). The graph represents the changes in the number of LDs/cell for LoVo and HT29 cell lines. Images were analysed using ImageJ for mean of LDs per cell. Comparisons between groups are shown with corresponding  $p$ -values (unpaired Student's  $t$ -test). Error bars represent the means  $\pm$  SD. LoVo:  $N = 532$  cells; HT29:  $N = 4645$  cells. (b) High-resolution transmission electron micrograph of sEVs isolated from HT29 media taken with Zeiss EM 910 at 100 kV. Uranyl acetate negative staining reveals that purified sEVs have a donut-shaped morphology. The diameter of sEVs ranged around 100 nm. The presented image has a magnification of 16000  $\times$  in TEM mode. The size bars on the image represent 150 nm. (c) Ratio of particle number per cell for the sEV fractions (F2) released by LoVo and HT29 by nanoparticle tracking analysis (NTA). Comparisons between groups are shown with corresponding  $p$ -value. Unpaired students  $t$ -test was performed. Error bars represent the means  $\pm$  SD from three independent experiments. (d) Western Blot for the sEV pellets (100K) obtained by differential ultracentrifugation combined with SEC for LoVo and HT29 cells. The same sample volume (19.5  $\mu$ L) was loaded onto the 10% acrylamide gel. The results presented here are representative of three independent experiments. The intensity of the bands corresponding to HT29 proteins was normalised by the intensity of the LoVo proteins band. Unpaired students  $t$ -test was performed. Error bars represent the means  $\pm$  SD from three independent experiments. (e) HT29 cells were stained with LD540 for LDs and sorted based on their 10% brightest and 10% dimmest LD540 fluorescence values. Thereafter, sorted HT29 cells were spun on slides using cytospin and were directly fixed, permeabilised and stained for CD63 (MVBs) and DAPI (nuclei). Cells were then imaged at the confocal microscope with a 100X objective (Leica Microsystems; Concord, Ontario, Canada). Displayed are the merged images of the CD63 and DAPI stainings (Scale bar, 20  $\mu$ m). \*  $\leq 0.05$ ; \*\*  $\leq 0.01$ ; \*\*\*  $\leq 0.001$  and \*\*\*\*  $\leq 0.0001$ .

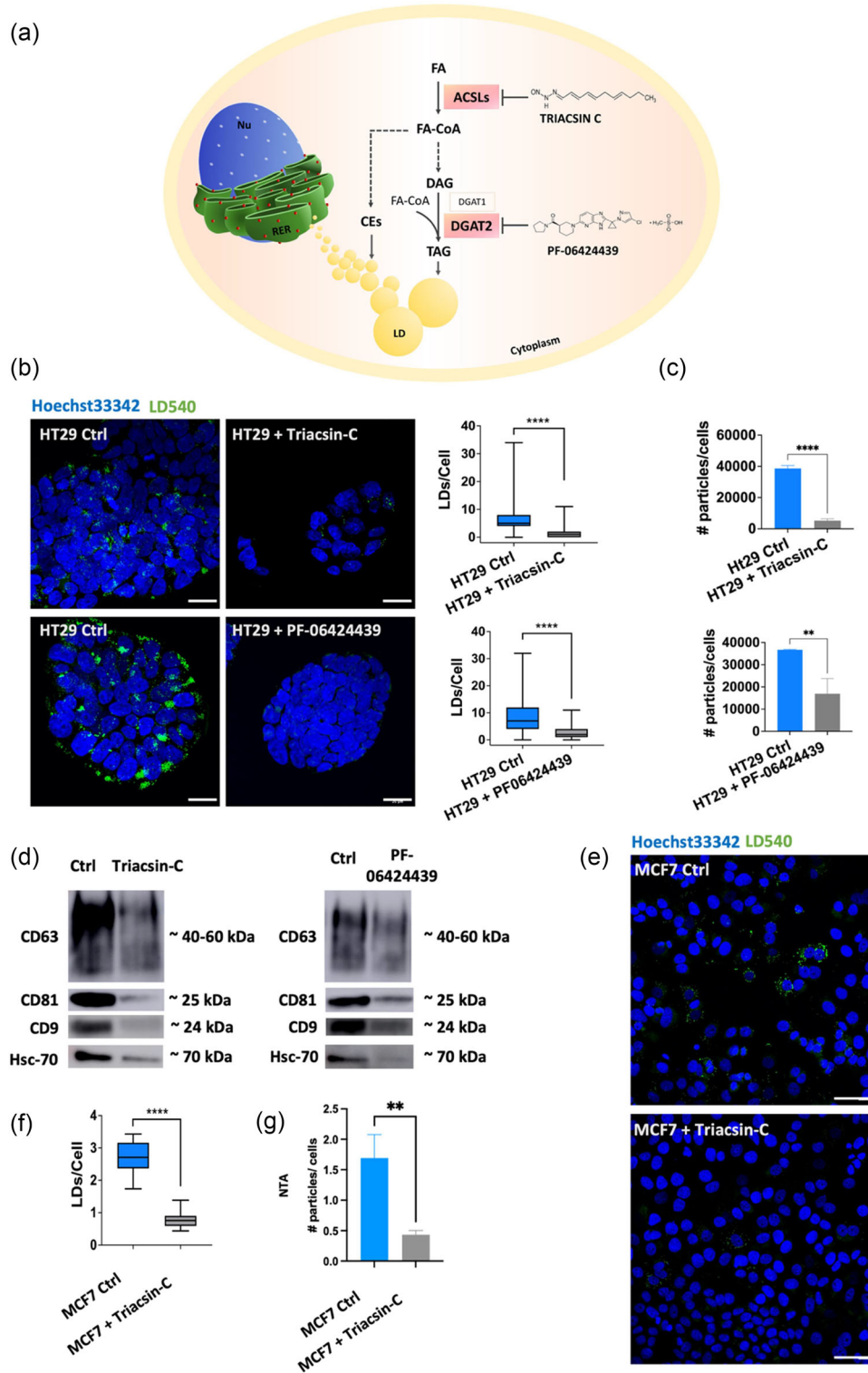


**FIGURE 2** LD inhibition reduces sEV release. (a) Representation of the mechanism of action for Triacsin C and PF-06424439. (b) HT29 cells control or treated, either with 10 μM Triacsin-C or 30 μM PF-06424439 for 72 h, were stained with LD540 (green) for LDs and DAPI (blue) for nuclei and imaged at the confocal microscope with a 100X objective (Leica Microsystems; Concord, Ontario, Canada). The pinhole was set for a slice thickness of 17.4 μm, with an interval between slices of 0.9 μm. Z-projection of the z-stack acquisitions is shown (left). The merged images of the LD540 and DAPI staining from one independent experiment are displayed (Scale bar, 20 μm). The graph represents the changes in the number of LDs/cell for HT29 cell line treated or not with one of the two inhibitors used in this experiment. Images were analysed using ImageJ for mean LDs per cell. Comparisons between groups are shown with corresponding *p*-values (unpaired Student's *t*-test). Error bars represent the means ± SD. (c) Ratio of particle number per cell for sEV fractions (F2) released by HT29 control or treated with LD inhibitors using NTA. Unpaired students *t*-test was performed. Error bars represent the means ± SD from three independent

(Continues)

**FIGURE 2** (Continued)

experiments. (d) Western Blot for the sEVs pellets (100K) obtained by differential ultracentrifugation combined with SEC for HT29 cells control or treated, either with Triacsin-C 10  $\mu\text{M}$  or PF-06424439 30  $\mu\text{M}$ . The same sample volume (19.5  $\mu\text{L}$ ) was loaded onto the 10% acrylamide gel. (e) MCF7 cells control or treated, either with 7.5  $\mu\text{M}$  Triacsin-C for 72 h, were stained with LD540 (green) for LDs and DAPI (blue) for nuclei and imaged at the confocal microscope with a 63X objective. The pinhole was set for a slice thickness of 17.4  $\mu\text{m}$ , with an interval between slices of 0.9  $\mu\text{m}$ . Z-projection of the z-stack acquisitions is shown (left). The merged images of the LD540 and DAPI staining from one independent experiment are displayed (Scale bar, 20  $\mu\text{m}$ ). The graph represents the changes in the number of LDs/cell for MCF7 cell line treated or not with Triacsin-C (7.5  $\mu\text{M}$ ). Images were analysed using ImageJ for mean LDs per cell. Comparisons between groups, reported in (f), are shown with corresponding *p*-values (unpaired Student's *t*-test). Error bars represent the means  $\pm$  SD. (g) Ratio of particle number per cell for sEV fractions (F2) released by MCF7 control or treated with Triacsin-C using NTA. Unpaired students *t*-test was performed. Error bars represent the means  $\pm$  SD from three independent experiments. \*  $\leq 0.05$ ; \*\*  $\leq 0.01$ ; \*\*\*  $\leq 0.001$  and \*\*\*\*  $\leq 0.0001$ .

of LD and sEV numbers per cell for PF-06424439. Both inhibitors induced a cellular LD number reduction 72 h after incubation, as shown by confocal analysis and the associated quantification (**Figure 2b**). The decrease of LD count observed after Triacsin-C or PF-06424439 treatments was correlated with a drop of CD63 expression in the cells (**Figure S2B**), a reduction of sEV released in the supernatant (**Figure 2c**) and a reduction of the protein concentration within the sEV fraction (**Figure S2C**). In addition, a lower protein expression of exosomal markers (CD9, CD63, CD81 and Hsc-70), as shown in **Figure 2d**, was observed 72 h after incubation with both inhibitors (**Figure 2d**). A quantification of exosomal marker expression was performed on three independent experiments emphasising the difference between the control and the treated conditions (**Figure S2D**). The results obtained in HT29 cell line were also confirmed in MCF7 cell line. In accordance with our first results, the LD inhibition with Triacsin-C (7.5  $\mu\text{M}$  for 72 h) (**Figure 2e,f**) reduced the number of sEVs released (**Figure 2g**) and the expression of exosomal markers in the sEV fraction (**Figure S2E**). Similar reduction was also observed for CD63 after Triacsin-C treatment in the cells (**Figure S2F**). Altogether, these results reinforce the connection between LDs and sEVs.

### 3.3 | Iron metabolism supports the connection between LDs and sEVs

After demonstrating that DGAT2 inhibition resulted in a decrease in the number of LDs/cell, thereby suggesting that LDs are upstream of sEV biogenesis, we sought to further support this evidence by modulating the LD count per cell (both increasing and decreasing) through various methods (see results reported in Figures 3, 4 and 5). To achieve this, we began by interfering with cellular iron metabolism. Indeed, it is now quite well established that there is an interplay between iron and lipid metabolisms. In a previous work (Tirinato et al., 2021), we demonstrated that Ferritin Heavy chain (FTH1)—a key enzyme involved in cytoplasmic iron storage and redox homeostasis—regulated the cellular LD count. Therefore, we thought to use the same experimental system, based on short hairpin RNA targeting FTH1 (shFTH1) or scrambled RNA (shRNA) in the MCF7 cell line, to evaluate the sEV biogenesis. First, we collected proteins from MCF7 shRNA and MCF7 shFTH1 to conduct a full proteome analysis. From this analysis, 543 proteins were found to be upregulated (Log2 Fold change  $>1.2$ ) and 770 proteins downregulated (Log2Fold  $< 0.833$ ) in MCF7 shFTH1 cells (**Figure 3a**). We then confirmed that metabolic pathways, including small molecule metabolic processes and cellular catabolic processes, were downregulated (**Figure S3A**) in MCF7 shFTH1 cells. Additionally, the expression of proteins involved in adipogenesis, fatty acid metabolism as well as lipoprotein and cholesterol synthesis, was mostly downregulated in MCF7 shFTH1 cells (**Figure S3B**). Further validation by RT-qPCR was performed on selected genes (STEAP3, TFRC, ANXA1, STX7) which resulted in accordance with the proteomic data (**Figure S3C**). In particular, 31 proteins involved in the lipid metabolism were upregulated whilst 46 proteins were downregulated in the MCF7 shFTH1 cell line. Using String and Cytoscape software, we found that the 'extracellular vesicle' pathway was downregulated, among others, in MCF7 shFTH1 cells (**Figure 3b**). A closer look to the exosomal pathway highlighted that 62.7% of proteins related to this pathway were downregulated in MCF7 shFTH1 cells compared to the MCF7 shRNA ones (**Figure 3c**). Several of the downregulated proteins participate in the synthesis processes whilst the upregulated ones are predominantly implicated either in protein/RNA targeting mechanisms or constitute surface proteins identifiable on sEVs.

In accordance with these results, NTA analysis emphasised fewer sEVs/cell released from MCF7 FTH1 cells as compared to MCF7 shRNA cells (**Figure 3d**). Similarly, we found more CD63<sup>+</sup> MVBs in MCF7 shRNA as compared to MCF7 shFTH1 cells (**Figure S3D**). By analysing the protein expression of exosomal markers (Annexin V, Flotillin-1, CD81 and CD9) on the same sEV sample volume, we evidenced a lower expression of those markers in MCF7 shFTH1 than in MCF7 shRNA cells (**Figure 3e**).

The proteomic results, strengthen this finding, as the expression of over half the exosomal markers was downregulated in MCF7 shFTH1 cells compared to MCF7 shRNA cells (**Figure 3f**). Altogether, these results confirm that sEV amount is directly correlated with cellular LD count and that iron metabolism is upstream of the LD-sEV connection.



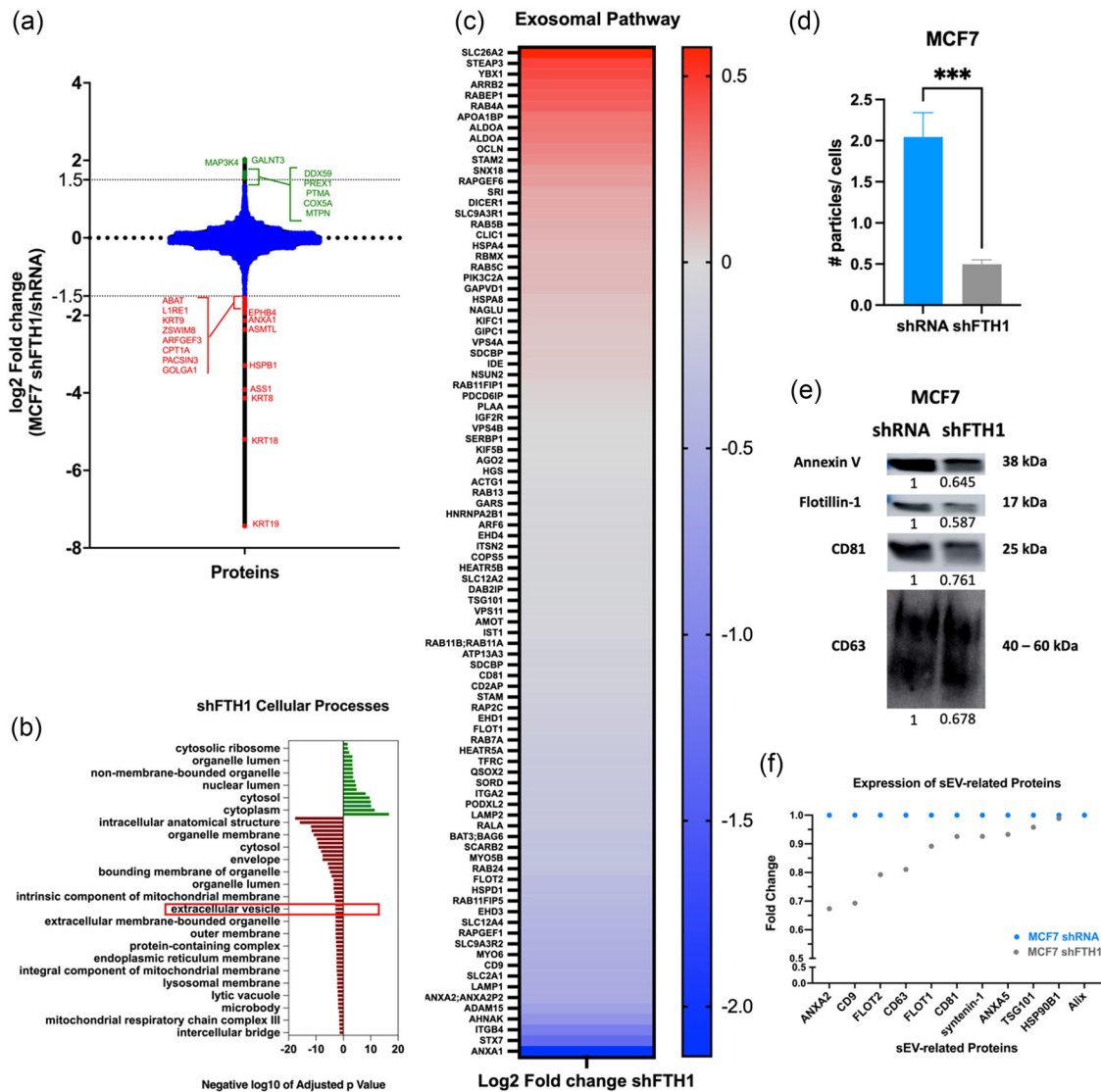


**FIGURE 3** Iron metabolism supports the connection between LD and sEVs (a) Violin plot depicting the ratio of  $\log_2$  Fold for MCF7 shFTH1/MCF7 shRNA. The proteins (red dots) for which the expression was highly upregulated (green) or highly downregulated (red) were annotated on the plot (b) Cellular processes upregulated (green) and downregulated (red) in MCF7 shFTH1 cells. (c) Heatmap of proteins belonging to the exosomal pathway within the MCF7 shFTH1/MCF7 shRNA cell system. Representation of  $\log_2$  Fold change values. (d) Ratio of particle number per cell for the sEV fraction (F2) released by MCF7 shRNA and MCF7 shFTH1 (F2), using NTA. Comparisons between groups are shown with corresponding *p*-value. Unpaired students *t*-test was performed. Error bars represent the means  $\pm$  SD from three independent experiments (*n* = 3). (e) Western Blot for the sEV pellets (100 K) obtained by differential ultracentrifugation combined with SEC for MCF7 shRNA and MCF7 shFTH1 cells. The same sample volume (19.5  $\mu$ L) was loaded onto the 10% acrylamide gel. Annexin V, Flotillin 1, CD81 and CD63 exosomal markers were used. An intensity quantification using ImageJ can be found under each band. (f) Expression of main exosomal markers (Annexin A2 (ANXA2), CD9, flotillin 2 (FLOT2), CD63, flotillin 1 (FLOT1), CD81, Syntenin-1, Annexin A5 (ANXA5), TSG101, HSP90B1 and Alix) is shown for MCF7 shRNA (blue) and MCF7 shFTH1 cells based on proteomic data (*n* = 1). \*  $\leq$  0.05; \*\*  $\leq$  0.01; \*\*\*  $\leq$  0.001 and \*\*\*\*  $\leq$  0.0001.

### 3.4 | LD stimulation increases sEV biogenesis

Since the LD inhibition led to a decrease of sEV release, we then decided to evaluate the LD-sEV connection in a context of LD stimulation. It has been previously reported by our research group and others that x-ray radiation (Nisticò et al., 2021; Tirinato et al., 2021) and acidosis (pH 6.5) (Corbet et al., 2020) promote an enrichment in cancer cells with a large number of LDs /cell. We thus chose to investigate the effect of pH variation on MCF7 and H460 cell lines. Both cell lines were incubated with neutral pH (7.4) or in acidic (pH 6.5) conditions for 72 h. Subsequently, the number of LDs per cell was assessed by confocal microscopy. We confirmed a higher number of LDs/cell in acidosis when compared to neutral media for both cell lines (Figure 4a). The sEV isolation revealed a higher number of particles released per cell (Figure 4b) and a higher protein concentration (Figure S4A) in low pH conditioned media. In line with these results, the expression of exosomal markers (CD63, CD9, CD81 and HSC-70) on sEVs isolated from acidic condition was more elevated than the neutral one (Figures 4c and S4B). The comparison between the two pH settings was carried out using the same sEV sample volume.



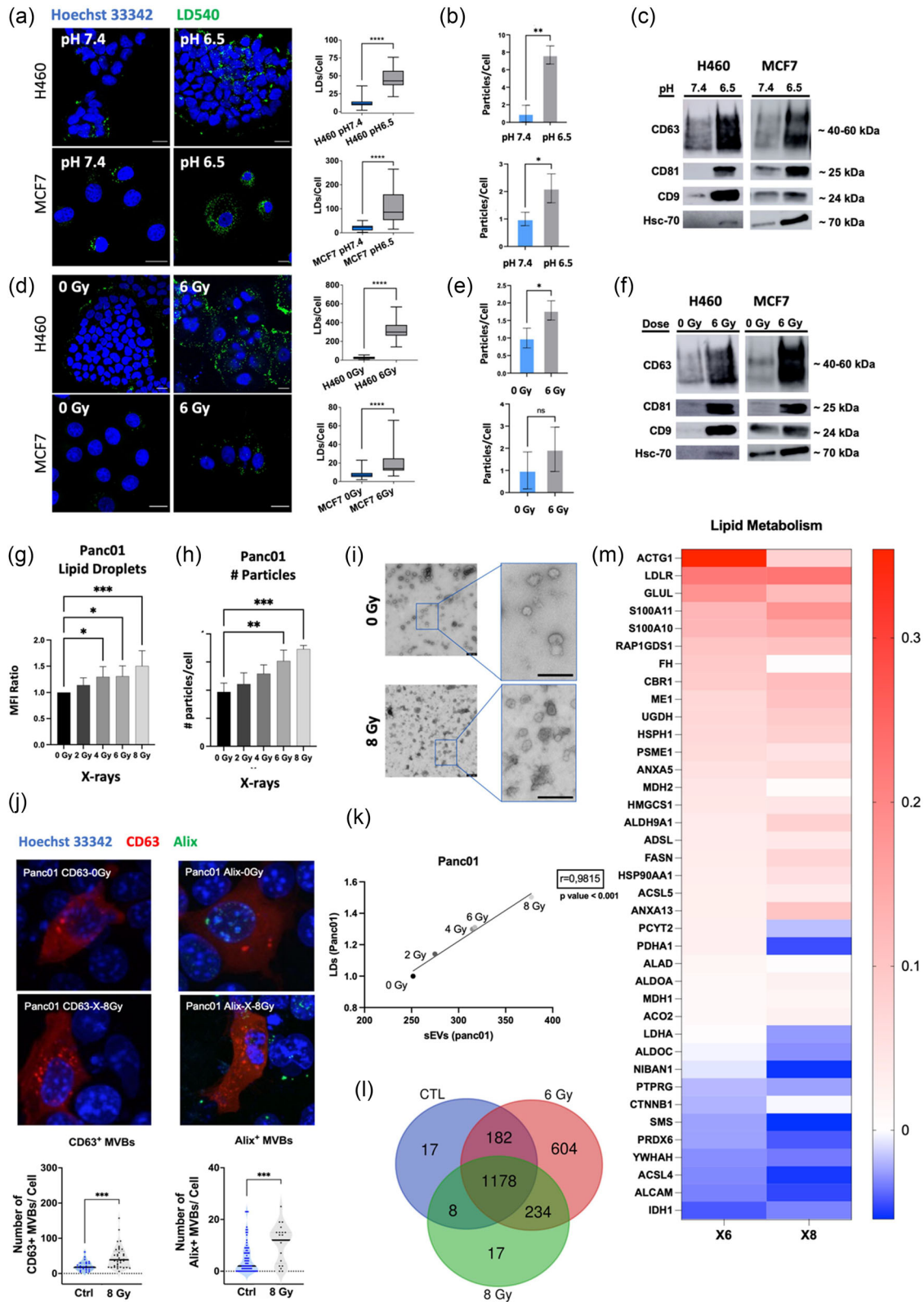


**FIGURE 4** LD stimulation increases sEV biogenesis (a) and (d) Treated (pH 6.5 (a) or 6 Gy (d)) and untreated (pH 7.4 (a) or 0 Gy (d)) H460 and MCF7 cells were stained with LD540 (yellow) for LDs and DAPI (blue) for nuclei and imaged at the confocal microscope with a 100X objective (Leica Microsystems; Concord, Ontario, Canada). Displayed are the merged images of the LD540 and DAPI staining (Scale bar, 20  $\mu$ m). The graph represents the changes in cellular LD count for MCF7 and H460 cell lines. Images were analysed using ImageJ for mean LDs per cell. Comparisons between groups are shown with corresponding  $p$ -values (unpaired Student's  $t$ -test). Error bars represent the means  $\pm$  SD. (b) and (e) Ratio of particle number per cell for the sEV fractions (F2) released by treated (pH 6.5 (b) or 6 Gy (e)) and untreated (pH 7.4 (b) or 0 Gy (e)) H460 or MCF7 cells, using NTA. Results from three independent experiments. Data are presented as means  $\pm$  SD. Comparisons between groups are shown with corresponding  $p$ -value (unpaired Student's  $t$ -test). (c) and (f) Western Blot for the

(Continues)

**FIGURE 4** (Continued)

sEVs pellets (100K) obtained by differential ultracentrifugation combined with SEC for H460 and MCF7. Same sample volume (19.5  $\mu$ L) was loaded onto the 10% acrylamide gel. The results presented here are representative of three independent experiments. (g) Panc01 cells, untreated and irradiated with 2, 4, 6 or 8 Gy, were stained with LD540 for LDs and PI for dead cells and analysed by flow cytometry. The graph represents the mean fluorescence intensity (MFI) (irradiated/unirradiated ratio). Comparisons between groups are shown with corresponding *p*-values (ANOVA I, Dunnett's post-test). Error bars represent the means  $\pm$  SD. *n* = 3. (h) Ratio of particle number per cell for sEV fraction (F2) released by Panc01 irradiated with x-rays (0, 2, 4, 6 or 8 Gy). Results from three independent experiments. Data are presented as means  $\pm$  SD. Comparisons between groups are shown with corresponding *p*-value (ANOVA I, Dunnett's post-test). (i) High-resolution transmission electron micrograph of sEVs isolated from unirradiated (0 Gy) or irradiated (8 Gy) Panc01 media taken with Zeiss EM 910 at 100 kV. Uranyl acetate negative staining reveals that purified sEVs have a cup-shaped morphology enclosed by a lipid bilayer. The diameter of sEVs is around 90–100 nm. The presented image has a magnification of 16000  $\times$  in TEM mode. The size bars on the image represent 250 nm. (j) Number of CD63<sup>+</sup> or ALIX<sup>+</sup> MVBs after irradiation (8 Gy) in Panc01 cells transfected CD63-pHLuorin or ALIX-mCherry plasmids (*n* = 1). (k) Pearson correlation on mean values was run to determine the relationship sEV and LD number. The correlation factor is 0.9907. (l) Venn diagram of sEV proteomics analysis. Comparison of the proteins regulated for x-ray irradiation (6 and 8 Gy) with respect to the proteomics analysis of sEVs obtained from unirradiated Panc01 cells. (m) Heatmap of proteins belonging to the lipid metabolism pathway within the sEV released by PANC01 cells x-ray irradiated (6, 8 Gy) compared to their non-irradiated counterpart. Representation of Log<sub>2</sub> Fold change values for 6 and 8 Gy x-rays. \*  $\leq$  0.05; \*\*  $\leq$  0.01; \*\*\*  $\leq$  0.001 and \*\*\*\*  $\leq$  0.0001.

The same approach was used to study the effects of radiation. In our previous work, we showed that cancer cells surviving to 6 Gy x-rays were characterised by an increase of the cellular LD count 72 h after irradiation (Nisticò et al., 2021; Tirinato et al., 2021). Starting from this premise, we confirmed those data in H460 and MCF7 cells and extended the study to Panc01 cell line, using either confocal imaging or flow cytometry (Figures 4d,g and S4C). Propidium iodide was used to ensure that dead cells (PI<sup>+</sup> cells) were not included in the flow cytometry analysis. Since the supernatant was replaced every 24 h and the percentage of PI<sup>+</sup> cells was very low (2.37%), we estimated that dead cells were washed away at the time of analysis (confocal microscopy or flow cytometry). Particle number and analysis of the exosomal marker expression (CD63, CD9, CD81 and HSC-70) demonstrated that irradiation treatment was also able to increase the sEV secretion (Figures 4e,f and S4D). Interestingly, the cellular LD count increased proportionally to the radiation dose given to the cells (Figures 4g and S5A), and we observed the same trend for sEVs release (Figure 4h). Moreover, there is a clear correlation between cellular LD count and sEV biogenesis, as represented in Figure 4k. EM also indicated the elevated number of sEVs collected from H460 and Panc01 72 h after 6 or 8 Gy x-rays respectively, as compared to the unirradiated conditions (Figures 4i and S5B). Interestingly, the particle size was similar between sEVs isolated from irradiated or unirradiated cells (Figure S5C). In addition, the analysis of CD63<sup>+</sup> or Alix<sup>+</sup> multivesicular bodies (MVBs) in unirradiated (0 Gy) or irradiated (8 Gy) pancreatic cancer cells revealed an increased number of MVBs after irradiation (Figure 4j).

Since irradiation induces cell death, including apoptosis and autophagy, it is important to consider that very small apoptotic bodies (100–1000 nm) and autophagic vesicles (40–1000 nm) might be co-isolated by differential ultracentrifugation combined with SEC (cut-off 200 nm) within the sEV pool. We therefore characterised the expression of Annexin V and LC3 on sEVs isolated from Panc01 irradiated cells via Western Blot (Figure S5E) and ELISA (Figure S5D), showing an increase expression of those markers. However, an immunogold EM-staining also showed that 71.63% of sEVs were coated by gold-coupled anti-CD63 antibodies in irradiated condition (8 Gy) (Figure S5F). Altogether, whilst we cannot exclude a contamination of our sEVs with small apoptotic and autophagic vesicles after irradiation, we showed that the expression of CD63 on sEVs (Western Blot), the number of CD63<sup>+</sup> sEVs (EM) and the number CD63<sup>+</sup> MVBs (confocal microscopy) were increased after irradiation, meaning that a higher proportion of CD63<sup>+</sup> vesicles were produced intracellularly and released in the supernatant.

Finally, to evaluate how irradiation could affect the exosomal cargos, exosomal proteins were extracted from sEVs either released by x-ray irradiated (6, 8 Gy) Panc01 cells or by their unirradiated counterpart. 431 sEV proteins, analysed by Mass Spectrometry (Figure 4l) were downregulated whilst 566 proteins had an upregulated expression compared to the unirradiated conditions. Interestingly, a closer look to the lipid metabolism pathway (Figure 4m) led us to identify a higher expression of proteins involved in lipid anabolism in sEVs derived from irradiated Panc01 as compared to the control condition, and especially after 6 Gy. The proteins, whose expression was downregulated, belonged to the lipid catabolism pathway, meaning that irradiation favours lipid biosynthesis whilst reducing lipolysis, in accordance with the increased LD formation. This also means that radiation, in addition to affect cellular LD count, regulated the lipid-related sEV proteome. This is of high interest since the exosomal lipid proteome and lipid profile modulate the invasiveness of the recipient cells (Cerezo-Magaña et al., 2021; Crewe & Scherer, 2022; Lazar et al., 2016).

Altogether, these results demonstrate that variations in the tumour microenvironment (e.g., pH) or treatments like conventional radiation can strongly stimulate LD biogenesis and similarly modulate the interconnected sEV pathway.

### 3.5 | Patient-derived colorectal cancer stem cells modulate their LD number and sEV release under hypoxia

It is known that LDs are considered as a functional marker for cancer stemness (Tirinato et al., 2017). Indeed, patient-derived CR-CSCs (Figure S6A) with a large number of LDs/cell exhibited a higher tumorigenic potential (Tirinato et al., 2017; Tirinato

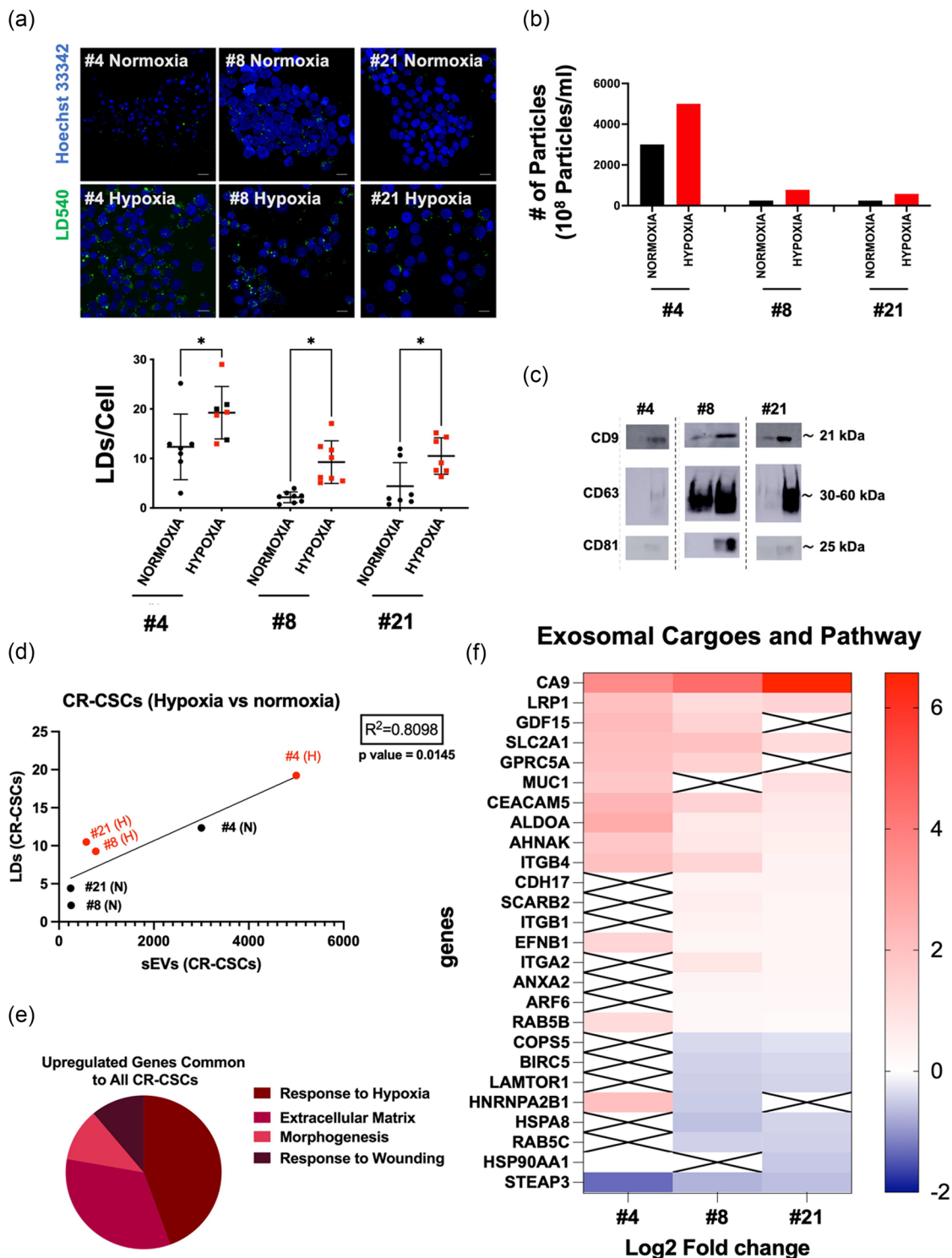


**FIGURE 5** Patient-derived colorectal cancer stem cells modulate their cellular LD count and sEV release in hypoxic condition. (a) LD quantification in Colorectal Cancer Stem Cells (CR-CSCs) derived from patients with colorectal cancer. Treated (Hypoxia, H) and untreated (Normoxia, N) CR-CSCs (#4, #21, #8) were stained with BODIPY 493/503 for LDs (green) and DAPI (blue) for nuclei and imaged at the confocal microscope with a 100X objective (Leica Microsystems; Concord, Ontario, Canada). The merged images of the BODIPY and DAPI staining from three independent experiments are displayed (Scale bar, 20  $\mu$ m). The graph represents the changes in cellular LD count for the different CR-CSCs in hypoxia as compared to normoxia. Images were analysed using ImageJ for mean LDs per cell. Comparisons between groups are shown with corresponding *p*-values (ANOVA I, Sidak post-test). Error bars represent the means  $\pm$  SD. \*  $\leq$  0.05; \*\*  $\leq$  0.01; \*\*\*  $\leq$  0.001 and \*\*\*\*  $\leq$  0.0001, *n* = 3. (b) Ratio of particle number per cell for sEV fraction (F2) treated (Hypoxia, H) and untreated (Normoxia, N) (F2) released by CR-CSCs ((#4, #21, #8) (*n* = 1)). (c) Western Blot for the sEVs pellets (100K) obtained by differential ultracentrifugation combined with SEC for all CR-CSCs. The sample volume (19.5  $\mu$ L) was loaded onto the 10% acrylamide gel. (d) Pearson correlation on mean values was run to determine the relationship sEV and LD number for CR-CSC when cellular LD count is either high (hypoxia) or low (normoxia). \*\*  $\leq$  0.05; \*  $\leq$  0.01; \*\*\*  $\leq$  0.001 and \*\*\*\*  $\leq$  0.0001. (e) Diagram of common upregulated pathways in all CR-CSCs culture under hypoxia (Cytoscape: Network

(Continues)



**FIGURE 5** (Continued)

specificity 6 genes, 0.4 k score,  $p$ -value adjusted  $< 0.05$ ,  $\log_2$  Fold change  $> 1.2$ ,  $n = 3$ ). (f) Heatmap of genes belonging to the exosomal pathway of the CR-CSCs cultured in different oxygen conditions (normoxia vs. hypoxia). Representation of  $\log_2$  Fold change values for the hypoxic condition as compared to the normoxic condition. The colour coding is applied only to genes that show significant differential expression (adjusted  $p$ -value  $< 0.1$ ), whilst non-significant genes remain uncoloured. The cross (X) means that the protein was not detected in the condition.

et al., 2015). Moreover, it was shown that restricted oxygen conditions increased the CSC fraction and promoted the acquisition of a stem-like state (Mylonis et al., 2019). Considering this, we decided to study the influence of hypoxia on the LD-sEV interconnection in patient-derived CR-CSCs. By using confocal microscopy, we observed a higher number of LDs/cell when CR-CSCs were cultured in hypoxic conditions as compared to the normoxic state (Figure 5a). Concurrently, NTA analysis revealed a higher number of sEVs released by CR-CSCs in hypoxic conditions compared to normoxic conditions (Figure 5b). The analysis of some exosomal markers also revealed a higher expression of CD9, CD63 and CD81 in hypoxia than in normoxia when the same sEV sample volume was used for Western Blotting (Figure 5c). Overall, we observed a clear correlation between cellular LD count and sEV number with a Pearson's  $r$  coefficient of 0.870 ( $p < 0.01$ ) (Figure 5d).

Finally, to further evaluate the effect of hypoxia on the lipid metabolism and the exosomal pathway, we collected mRNA from the three different CR-CSCs in normoxia and hypoxia for a full transcriptome analysis. This led us to identify four upregulated pathways under hypoxic conditions using String and Cytoscape: i) response to hypoxia; ii) extracellular matrix; iii) morphogenesis; iv) response to wounding (Figure 5e).

Downregulated genes belonged to i) tRNA pathway and ii) positive regulation of double strand break repair via homologous recombination (Figure S6B). This analysis also allowed us to confirm that many of the genes involved in the sEV cargoes and pathway were upregulated (Figure 5f) similarly as the sEV number was modulated in the three CR-CSCs (Figure 5b). Interestingly, the expression of the genes involved in the lipid metabolic pathways was mainly upregulated under hypoxia, for all CR-CSCs (Figure S6C). In general, downregulated lipid metabolism-related genes were associated with lipid catabolism whilst the upregulated ones were associated with lipid anabolism. As expected, the hypoxia pathway was also upregulated in CR-CSCs cultured under hypoxic conditions as compared to the normoxic ones (Figure S6D). Overall, these results demonstrated that the interconnection between LDs and sEVs was also observed in patient-derived CR-CSCs cultured in hypoxic conditions.

### 3.6 | RAB 5C as one of the regulators of the LD—sEV axis

Based on our proteomic analyses, we identified proteins whose expression was modulated based on cellular LD count. Focusing on proteins involved in the exosomal pathway, we identified a potential role for RAB18, RAB5C and RAB7A in the interconnection between LDs and sEVs. (Figure S7A; Table S1). We therefore decided to use RNA silencing to target these three genes and verified through Western Blot that targeting RAB18, RAB5C and RAB7A affected protein expression 72 h after transfection (Figure S7B). The RAB18 and RAB7A, but not RAB5C, gene silencing impacted the LD count in HT29 cells. Indeed, the number of LDs increased in HT29 cells transfected with siRNAs (#1, #2 and #3 sequences) against RAB18, whilst it decreased with siRNAs targeting RAB7A (#1, #2 and #3 sequences) (Figure 6a). The same trend was observed for the sEV counterpart when using NTA (Figure 6b): the number of released sEVs increased with siRNA RAB18 (Figure S7C) and decreased with siRNA RAB7A (Figure S7D). However, the expression of several sEV markers (CD63, CD81, CD9 and Hsc-70) was mostly unchanged by the targeting of RAB18 or RAB7A (Figure S7E, S7F). This suggests that a putative connection between LDs and sEVs was not disrupted by the targeting of RAB18 and RAB7A. On the contrary, whilst the number of LDs/cell was not modified by targeting RAB5C with siRNAs (#1, #2 and #3 sequences) (Figure 6a), the number of sEVs released and the expression of sEV markers were reduced (Figure 6b–d), meaning that the LD-sEV connection was, at least in part, interrupted by inhibiting RAB5C expression level. Indeed, our data seem suggesting that RAB5C acts downstream of LDs and upstream of sEVs thus indicating a link between LDs and the sEV pathway.

To further determine whether this connection is direct or potentially regulated through other organelles, we also evaluated the impact of the number of LDs/cell on the lysosomal compartments (Figure S8A). Our findings suggested that HT29 LD<sup>High</sup> cells contained a smaller lysosomal network than HT29 LD<sup>Low</sup>, indicating that the lysosomal compartment is inversely proportional to the cellular LD count. To further investigate these results, a correlation graph was created (Figure S8B). The difference in lysotracker between HT29 LD<sup>High</sup> and HT29 LD<sup>Low</sup> cells expanded as the number of LDs increased. The  $R^2$  for this model was quite small (~5%), suggesting that although the number of LDs is correlated with the lysotracker area, it does not account for much of the variability in lysotracker (Figure S8A and S8B). In parallel, we assessed the protein expression of RAB7A, regulating the late endosome pathway (Figure S8C). The expression of RAB7s was, in most of the cases, directly correlated with the cellular LD count and number of sEV released. However, by targeting RAB5C, we did not observe a change in RAB7A protein expression (Figure S8D). This indicates that by interrupting the LD—sEV connection, partially, siRNA against RAB5C did not disturb the regulator of the late endosome pathway, RAB7A.

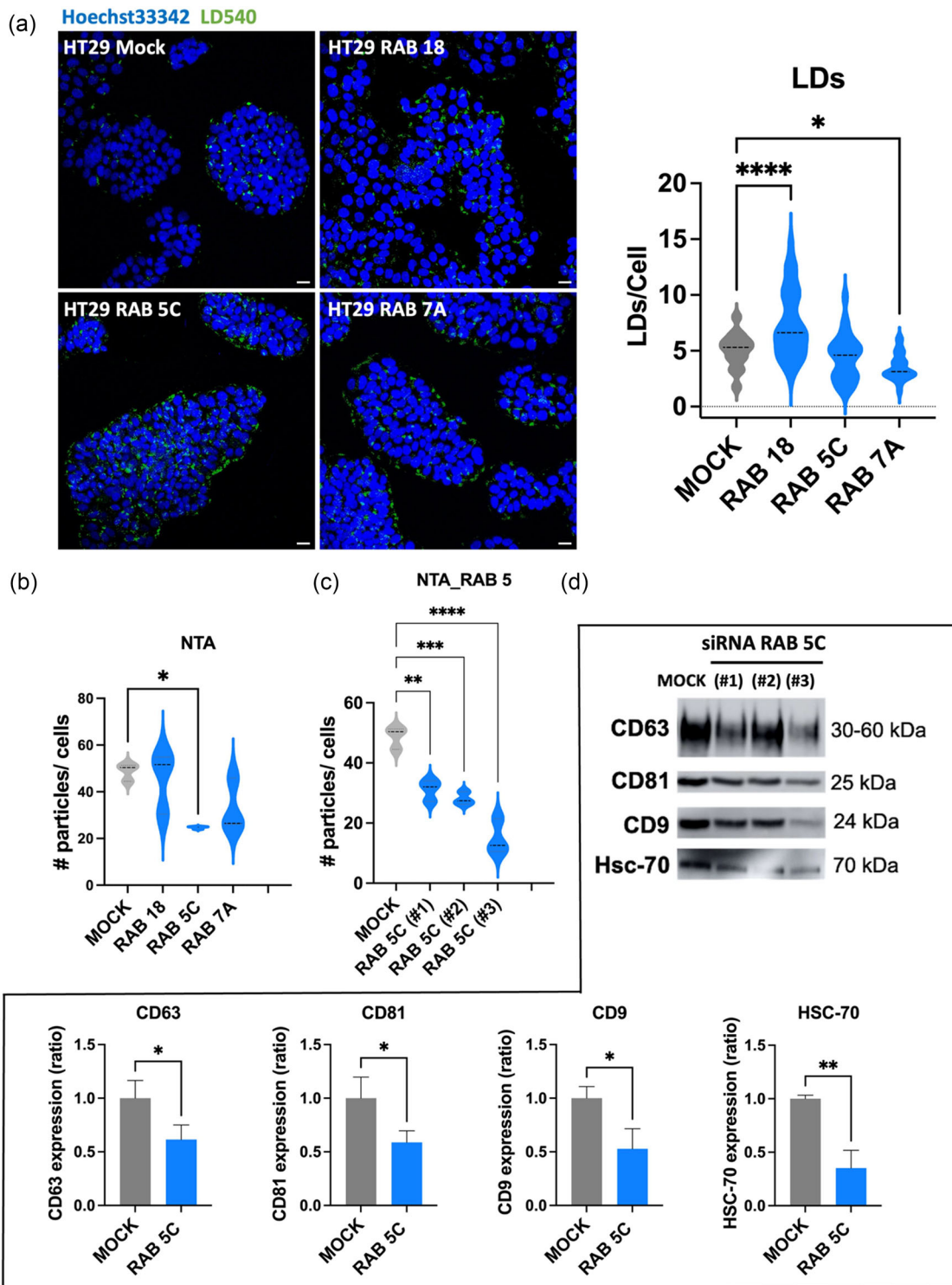


**FIGURE 6** RAB5C, but not RAB18 or RAB7A, is involved in the LD-sEV connection. (a) HT29 cell lines transfected either with siRNA MOCK (control) or targeted against RAB18, RAB5C or RAB7A were stained with LD540 (green) for LDs and DAPI (blue) for nuclei and imaged with a confocal microscope provided with a 100X objective (Leica Microsystems; Concord, Ontario, Canada). Z-projection of the z-stack acquisitions is shown (left). Displayed are the merged images of the LD540 and DAPI staining (Scale bar, 20  $\mu$ m). The graph represents the changes in number of LDs/cell for the different conditions. Images were analysed using ImageJ for mean of LDs per cell. For each RAB gene (RAB18, RAB5C and RAB7A), three different sequences (#1, #2 and #3) were used and the average LDs/cell for each sequence was considered for the statistical analysis. Comparisons between groups are shown with corresponding *p*-values (unpaired Student's *t*-test). Error bars represent the means  $\pm$  SD. (b) Ratio of particle number per cell for the sEV fractions (F2) released by HT29 transfected either with siRNA MOCK or with three different sequences (A, B, C) targeting either RAB18, RAB5C or RAB7A by NTA. Two-way ANOVA was performed and comparisons between groups are shown with corresponding *p*-value. Error bars represent the means  $\pm$  SD from three independent experiments. For each RAB gene (RAB18, RAB5C and RAB7A), three different sequences (#1, #2, #3) were used in a grouped statistical analysis (c) Ratio of particle number per cell for the sEV fractions (F2) released by HT29 transfected either with siRNA MOCK or with three different sequences (#1, #2, #3)

(Continues)



**FIGURE 6** (Continued)

targeting RAB5C by NTA. ANOVA I was performed and comparisons between groups are shown with corresponding *p*-value. Error bars represent the means  $\pm$  SD from three independent experiments. (d) Western Blot for the sEV pellets (100K) obtained by differential ultracentrifugation combined with SEC for HT29 cells transfected either with MOCK or with three different sequences against RAB5C. The same sample volume (19.5  $\mu$ L) was loaded onto the 10% acrylamide gel. The results presented here are representative of three independent experiments and were quantified with ImageJ. The intensity of the bands was normalised by the intensity of the HT29 MOCK band. Unpaired students *t*-test was performed. Error bars represent the means  $\pm$  SD from three independent experiments. Displayed are the merged images of the CD63 and DAPI stainings (Scale bar, 20  $\mu$ m). \*  $\leq$  0.05; \*\*  $\leq$  0.01; \*\*\*  $\leq$  0.001 and \*\*\*\*  $\leq$  0.0001. Comparisons without label must be considered not significant.

Finally, the expression of GM130, a regulator of the Golgi apparatus, has been evaluated as well. Studies have shown that GM130 interacts with proteins involved in lipid metabolism and trafficking, suggesting its involvement in LD biology (Song et al., 2022). However, there is limited evidence indicating a potential connection between GM130 and sEVs. Unfortunately, our data were unable to provide new and interesting insights into the role of GM130 in the connection between LDs and sEVs (Figure S8E). Furthermore, its expression under the tested conditions (LoVo, HT29, HT29 + Triacsin-C, HT29 + DGAT2 inhibitor, HT29 LD<sup>High</sup>, HT29 LD<sup>Low</sup>, PANC01 0 Gy and PANC01 Gy) did not exhibit a consistent trend (Figure S8E).

Although more experiments are needed to elucidate fully the involvement of the lysosomes and the endosomal system, it seems that the endosomes could take part in the LD-sEV connection. Nevertheless, this role might not imply RAB5C.

## 4 | DISCUSSION

By modulating cellular LD levels, either through inhibition of LD metabolism or stimulation of LD biosynthesis in different cancer cell types, we report for the first time a strong correlation between intracellular LD count numbers and sEV release. These findings were also validated in patient-derived CR-CSCs, demonstrating that hypoxia increased intracellular LDs as well as sEV biogenesis. Additionally, multiple omics data confirmed, at both mRNA and protein levels, that LD and sEV pathways were similarly modulated and closely connected. Even if a clear and robust mechanistic process behind this connection needs to be fully elucidated, our data suggest RAB5C as a potential candidate in establishing this cellular correlation.

There is growing evidence that LDs are not static organelles exclusively involved in safely storing excessive and dangerous lipids. Indeed, recent data have shown an intriguing role for LDs as lipid sources for potential membrane-shaped vesicles. Whilst the direct LD-sEV connection has never been made so far, hypoxia (Mylonis et al., 2019; Venturella et al., 2021), low pH (6.5) (Ban et al., 2015; Corbet et al., 2020; Logozzi et al., 2018), irradiation (Tirinato et al., 2021; Yu et al., 2006), reactive oxygen species (ROS) (Chiaradia et al., 2021; Jin et al., 2018), high glucose consumption (da Silva Novaes et al., 2019; Tirinato et al., 2019; Zhu et al., 2019) and cellular senescence (Flor et al., 2017; Takasugi, 2018), among others, have been shown to increase intracellular LD count as well as sEV release by cells. Several studies contributed to elucidate the mechanism behind the increased sEV biogenesis upon these stimulations. For example, cellular senescence and DNA damaging reagents or radiation were shown to stimulate sEV production through the activation of p53, at least partially (Lehmann et al., 2008). Intriguingly, p53 is known to activate the expression of several genes involved in endosome regulation, including RAB5B, Caveolin-1, TSAP6 and Champ4C (a subunit of ESCRT-III) (Wells et al., 2003; Yu et al., 2009). In parallel, p53 was also demonstrated to have an impact on the lipid and iron metabolisms (Laubach et al., 2021). Another example is the regulation of sEV release through ATM activation of the autophagic pathway in hypoxia (Xi et al., 2021). Hypoxia also triggers LD formation and sEV release through HIF1 $\alpha$  stabilisation. However, despite their multiple targets, p53 and HIF1 $\alpha$  are not sufficient to fully elucidate the link between LDs and the exosome pathway (Muñiz-García et al., 2022).

In other experiments, we demonstrated that FTH1 silencing, a protein involved in iron storage, reduced both LD count and sEV release in MCF7 cells. Elevated iron levels are associated with ferroptosis, a type of regulated cell death. Interestingly, ferritin plays a crucial role in Fe<sup>2+</sup> storage (Tang et al., 2021), and low amounts of ferritin drive ferroptosis. Since lipid peroxidation induces ferroptosis (Lu et al., 2021), cells protect themselves by storing lipids within LDs. As a result, resistance to ferroptosis is typically associated with LD accumulation. Another way for cells to cope with elevated iron levels is to promote its export, either through free secretion or via the exosome pathway when associated with ferritin. Indeed, high iron levels can trigger CD63 expression via the IRE-IRP pathway and promote exosomal secretion of ferritin-associated iron (Yanatori et al., 2021). In the same context, prominin 2 also facilitates the exosomal transport of ferritin (Brown et al., 2019). However, the IRE-IRP pathway and Prominin-2 are not sufficient to fully explain the LD-sEV connection.

RAB GTPases play a crucial role in coordinating endosomal trafficking, as they regulate vesicle budding, motility and tethering to the target compartment. Additionally, they provide transport specificity and organelle identity. In this study, we identified RAB5C as a significant factor in the LD-sEV connection. RAB5, a master regulator of early endosome biogenesis, has three isoforms—RAB5A, B and C—each with overlapping yet distinct functions. Alongside RAB5, we also evaluated the impact of RAB18 and RAB7A on the LD-sEV connection. Among the three RAB proteins we selected, the relationship between LDs and RAB18 is the most well-defined in the literature. In fact, RAB18 knockout has been shown to affect LD growth and maturation,

resulting in fewer but larger LDs (Li et al., 2017; Xu et al., 2018). Although RAB18 does not appear to be involved in LD biogenesis, its role in connecting LD catabolism to the autophagic and endosomal pathways is increasingly evident (Coulter et al., 2018; Gillingham et al., 2014). Interestingly, RAB18 KO cells exhibited increased expression and phosphorylation of ATG2 A/B, ATG9A and ATG16L1 as compensation for limited lipid availability (Coulter et al., 2018). Furthermore, since RAB3GAP1/2 controls RAB18's activity and location, its knockout affects LD count similarly to RAB18 KO (Coulter et al., 2018; Gillingham et al., 2014). RAB18's activity and location on LDs are also regulated by another complex, COPI-TRAPP II (TRAPPC9/TRAPPC10). However, TRAPP II does not appear to play a critical role in the early secretory pathway (Hodges and Wu, 2010). Lastly, RAB18 was found on a subtype of sEVs, the secretion of which is mediated by CHMP1A, an ESCRT-III protein (Coulter et al., 2018; Takasugi, 2018).

Whilst the relationships between other RAB proteins and the LD and sEV pathways haven't been thoroughly investigated, the emerging significance of RAB5C and RAB7A in these pathways is becoming apparent. For instance, mutations in RAB18, as well as RAB5, are known to cause Warburg syndrome, characterised by fewer but larger LDs (Xu et al., 2018). Proteomic data published several years ago also highlighted RAB5B, RAB7A and RAB18 as significant contributors to the connection between LDs and endoplasmic membranes (Gillingham et al., 2014). Hypoxia has been shown to increase exosome release via RAB5A (Deepa et al., 2018). Additionally, aromatase inhibitors, through the increased expression of RAB18, RAB5C and RAB7A, stimulate exosome biogenesis (Augimeri et al., 2020; Keerthikumar et al., 2015). Finally, investigation of CD63 routes revealed its interaction with RAB5 and RAB7 (Mathieu et al., 2021). Overall, whilst the literature provides insights supporting our findings of RAB5C as a potential factor in the LD-sEV connection, further research is needed to fully elucidate this relationship.

Adipocytes, due to their high LD volume occupancy, provide an ideal model for examining the relationship between LDs and sEVs. Notably, adipocytes from obese mice released more sEVs than those from lean mice (Clement et al., 2020). Obesity is associated with a higher risk of carcinogenesis in various organs, including breast, prostate, colon and liver (Lengyel et al., 2018). It also correlates with faster cancer progression and increased mortality (Lengyel et al., 2018). Interestingly, it has been shown that the fatty acid oxidation (FAO)-related protein content of adipocyte-derived sEVs alters mitochondrial dynamics in recipient melanoma cells, thereby promoting melanoma migration and aggressiveness (Lazar et al., 2016; Mutschelknaus et al., 2017). Similarly, adipocyte-derived sEVs, by transporting neutral lipids, induced an adipose-tissue macrophage phenotype in bone marrow.

In this study, we demonstrated that sEVs derived from irradiated cells exhibited a more robust lipid biosynthesis profile. Further analysis will help determine whether the lipid profile of sEVs released by cancer cells with low or high LD counts also influences the aggressiveness and metastatic state of targeted cancer cells.

In conclusion, targeting LDs or RAB5C to fine-tune sEV biogenesis could significantly impact the quantity, cargo and properties of sEVs. Investigating whether this connection is direct or mediated through other organelles will require further investigation and help uncover the complete mechanism behind the LD-sEV interaction. This understanding may pave the way for developing future patient-tailored therapies.

## AUTHOR CONTRIBUTIONS

**Geraldine C. Genard:** conceptualization; methodology; data curation; validation; formal analysis; investigation; writing original draft. **Luca Tirinato:** conceptualization; methodology; data curation; validation; formal analysis; investigation; writing original draft; funding acquisition; project administration; supervision. **Francesca Pagliari:** Methodology; investigation. **Jessica Da Silva:** Methodology; investigation. **Alessandro Giammona:** Methodology; investigation. **Fatema Alquraish:** Methodology; investigation. **Maria Parra Reyes:** Investigation. **Marie Bordas:** Methodology; investigation. **Maria Grazia Marafioti:** Methodology; investigation. **Simone Di Franco:** Data curation. **Jeanette Jansen:** Data curation. **Daniel Garcia:** Data curation. **Rachel Hanley:** Clelia Nisticò. Data curation. **Yoshinori Fukusawa:** Data curation. **Torsten Müller:** Data curation. **Jeroen Krijgsveld:** Data curation. **Matilde Todaro:** Supervision; investigation; funding acquisition. **Francesco Saverio Costanzo:** Supervision; investigation; funding acquisition. **Giorgio Stassi:** Supervision; investigation; funding acquisition. **Kendra K Mass:** Supervision; investigation; funding acquisition. **Michelle Nessling:** Data curation; validation. **Karsten Richter:** Data curation; validation. **Carlo Liberale:** Project supervision; funding acquisition; data curation; draft revision. **Joao Seco:** Conceptualisation; methodology; funding acquisition; project supervision; draft revision.

## ACKNOWLEDGEMENTS

We gratefully acknowledge the imaging and FACS Facilities at the DKFZ and the CoreLab Genomic Facility at KAUST for their prompt and precious support. We also are grateful to the Dr. Sebastian Dieter's group for the continuous access to the ultracentrifuge. Carlo Liberale and Joao Seco acknowledge funding from King Abdullah University of Science and Technology, Grant Award Number: OSR-CRG2018-3747. Luca Tirinato has received funding from AIRC and from the European Union's Horizon 2020 Research and Innovation Programme under the Marie Skłodowska-Curie grant agreement no. 800924. Jeannette Jansen was supported by grants of the German-Israeli Helmholtz Research School in Cancer Biology—Cancer Transitional and Research Exchange Program (Cancer-TRAX). Daniel Garcia-Calderon was funded by the Graduate School Scholarship Programme, 2019 from the DAAD.

## CONFLICT OF INTEREST STATEMENT

All authors declare no conflict of interest.

## DATA AVAILABILITY STATEMENT

Data available on request from the authors.

## ORCID

Géraldine C. Genard  <https://orcid.org/0000-0002-9495-0335>

Luca Tirinato  <https://orcid.org/0000-0001-9826-2129>

Carlo Liberale  <https://orcid.org/0000-0002-5653-199X>

## REFERENCES

- Aboumrad, M. H., Horn, R. C., Jr, & Fine, G. (1963). Lipid-secreting mammary carcinoma. Report of a case associated with Paget's disease of the nipple. *Cancer*, *16*, 521–525. [https://doi.org/10.1002/1097-0142\(196304\)16:4<521::aid-cnrc2820160414>3.0.co;2-b](https://doi.org/10.1002/1097-0142(196304)16:4<521::aid-cnrc2820160414>3.0.co;2-b)
- Augimeri, G., la Camera, G., Gelsomino, L., Giordano, C., Panza, S., Sisci, D., Morelli, C., Gyórfy, B., Bonofiglio, D., Andò, S., Barone, I., & Catalano, S. (2020). Evidence for enhanced exosome production in aromatase inhibitor-resistant breast cancer cells. *International Journal of Molecular Sciences*, *21*(16), 5841. <https://doi.org/10.3390/ijms21165841>
- Bailey, A. P., Koster, G., Guillermier, C., Hirst, E. M., MacRae, J. I., Lechene, C. P., Postle, A. D., & Gould, A. P. (2015). Antioxidant role for lipid droplets in a stem cell niche of drosophila. *Cell*, *163*(2), 340–353. <https://doi.org/10.1016/j.cell.2015.09.020>
- Ban, J. J., Lee, M., Im, W., & Kim, M. (2015). Low pH increases the yield of exosome isolation. *Biochemical and Biophysical Research Communications*, *461*(1), 76–79. <https://doi.org/10.1016/j.bbrc.2015.03.172>
- Bonifacino, J. S. (2014). Vesicular transport earns a Nobel. *Trends in Cell Biology*, *24*(1), 3–5. <https://doi.org/10.1016/j.tcb.2013.11.001>
- Bordas, M., Genard, G., Ohl, S., Nessling, M., Richter, K., Roider, T., Dietrich, S., Maaß, K. K., & Seiffert, M. (2020). Optimized protocol for isolation of small extracellular vesicles from human and murine lymphoid tissues. *International Journal of Molecular Sciences*, *21*(15), 5586. <https://doi.org/10.3390/ijms21155586>
- Brown, C. W., Amante, J. J., Chhoy, P., Elaimy, A. L., Liu, H., Zhu, L. J., Baer, C. E., Dixon, S. J., & Mercurio, A. M. (2019). Prominin2 drives ferroptosis resistance by stimulating iron export. *Developmental Cell*, *51*, 575–586.e4.
- Cerezo-Magaña, M., Christianson, H. C., van Kuppevelt, T. H., Forsberg-Nilsson, K., & Belting, M. (2021). Hypoxic induction of exosome uptake through proteoglycan-dependent endocytosis fuels the lipid droplet phenotype in glioma. *Molecular Cancer Research : MCR*, *19*(3), 528–540. <https://doi.org/10.1158/1541-7786.MCR-20-0560>
- Chiaradia, E., Tancini, B., Emiliani, C., Delo, F., Pellegrino, R. M., Tognoloni, A., Urbanelli, L., & Buratta, S. (2021). Extracellular vesicles under oxidative stress conditions: biological properties and physiological roles. *Cells*, *10*(7), 1763. <https://doi.org/10.3390/cells10071763>
- Clement, E., Lazar, I., Attané, C., Carrié, L., Dauvillier, S., Ducoux-Petit, M., Esteve, D., Menneteau, T., Moutahir, M., le Gonidec, S., Dalle, S., Valet, P., Burlet-Schiltz, O., Muller, C., & Nieto, L. (2020). Adipocyte extracellular vesicles carry enzymes and fatty acids that stimulate mitochondrial metabolism and remodeling in tumor cells. *The EMBO Journal*, *39*. <https://doi.org/10.15252/embj.2019102525>
- Corbet, C., Bastien, E., Santiago de Jesus, J. P., Dierge, E., Martherus, R., Vander Linden, C., Doix, B., Degavre, C., Guilbaud, C., Petit, L., Michiels, C., Dessy, C., Larondelle, Y., & Feron, O. (2020). TGFβ2-induced formation of lipid droplets supports acidosis-driven EMT and the metastatic spreading of cancer cells. *Nature Communications*, *11*(1), 454. <https://doi.org/10.1038/s41467-019-14262-3>
- Cotte, A. K., Aires, V., Fredon, M., Limagne, E., Derangère, V., Thibaudin, M., Humblin, E., Scagliarini, A., de Barros, J. P., Hillon, P., Ghiringhelli, F., & Delmas, D. (2018). Lysophosphatidylcholine acyltransferase 2-mediated lipid droplet production supports colorectal cancer chemoresistance. *Nature Communications*, *9*(1), 322. <https://doi.org/10.1038/s41467-017-02732-5>
- Coulter, M. E., Dorobantu, C. M., Lodewijk, G. A., Delalande, F., Cianferani, S., Ganesh, V. S., Smith, R. S., Lim, E. T., Xu, C. S., Pang, S., Wong, E. T., Lidov, H. G. W., Calicchio, M. L., Yang, E., Gonzalez, D. M., Schlaeger, T. M., Mochida, G. H., Hess, H., Lee, W. C. A., ... Walsh, C. A. (2018). The ESCRT-III Protein CHMP1A Mediates Secretion of Sonic Hedgehog on a Distinctive Subtype of Extracellular Vesicles. *Cell Reports*, *24*, 973–986.e8.
- Crewe, C., & Scherer, P. E. (2022). Intercellular and interorgan crosstalk through adipocyte extracellular vesicles. *Reviews in Endocrine & Metabolic Disorders*, *23*(1), 61–69. <https://doi.org/10.1007/s11154-020-09625-x>
- Cruz, A. L. S., Barreto, E. A., Fazolini, N. P. B., Viola, J. P. B., & Bozza, P. T. (2020). Lipid droplets: Platforms with multiple functions in cancer hallmarks. *Cell Death & Disease*, *11*(2), 105. <https://doi.org/10.1038/s41419-020-2297-3>
- da Silva Novaes, A., Borges, F. T., Maquigussa, E., Varela, V. A., Dias, M. V. S., & Boim, M. A. (2019). Influence of high glucose on mesangial cell-derived exosome composition, secretion and cell communication. *Scientific Reports*, *9*(1), 6270. <https://doi.org/10.1038/s41598-019-42746-1>
- De Maio, A. (2011). Extracellular heat shock proteins, cellular export vesicles, and the stress observation system: A form of communication during injury, infection, and cell damage. It is never known how far a controversial finding will go! Dedicated to Ferruccio Ritossa. *Cell Stress & Chaperones*, *16*(3), 235–249. <https://doi.org/10.1007/s12192-010-0236-4>
- Deepa, K., Dorayappan, P., Wanner, R., Wallbillich, J. J., Saini, U., Zingarelli, R., Suarez, A., Cohn, D., & Selvendiran, K. (2018). Hypoxia-induced exosomes contribute to a more aggressive and chemoresistant ovarian cancer phenotype: a novel mechanism linking STAT3/Rab proteins. *Oncogene*, *37*, 3806–3821.
- Ewels, P., Magnusson, M., Lundin, S., & Käller, M. (2016). MultiQC: Summarize analysis results for multiple tools and samples in a single report. *Bioinformatics (Oxford, England)*, *32*(19), 3047–3048. <https://doi.org/10.1093/bioinformatics/btw354>
- Flaherty, S. E., 3rd, Grijalva, A., Xu, X., Ables, E., Nomani, A., & Ferrante, A. W., Jr (2019). A lipase-independent pathway of lipid release and immune modulation by adipocytes. *Science (New York, N.Y.)*, *363*(6430), 989–993. <https://doi.org/10.1126/science.aaw2586>
- Flor, A. C., Wolfgeher, D., Wu, D., & Kron, S. J. (2017). A signature of enhanced lipid metabolism, lipid peroxidation and aldehyde stress in therapy-induced senescence. *Cell Death Discovery*, *3*, 17075. <https://doi.org/10.1038/cddiscovery.2017.75>
- Gillingham, A. K., Sinka, R., Torres, I. L., Lilley, K. S., & Munro, S. (2014). Toward a Comprehensive Map of the Effectors of Rab GTPases. *Developmental Cell*, *31*, 358.
- Hashemi, H. F., & Goodman, J. M. (2015). The life cycle of lipid droplets. *Current Opinion in Cell Biology*, *33*, 119–124. <https://doi.org/10.1016/j.ceb.2015.02.002>
- Heddleston, J. M., Li, Z., Lathia, J. D., Bao, S., Hjelmeland, A. B., & Rich, J. N. (2010). Hypoxia inducible factors in cancer stem cells. *British Journal of Cancer*, *102*, 789–795. Preprint at <https://doi.org/10.1038/sj.bjc.6605551>



- Hodges, B. D. M., & Wu, C. C. (2010). Proteomic insights into an expanded cellular role for cytoplasmic lipid droplets. *Journal of Lipid Research*, *51*, 262.
- Jeppesen, D. K., Fenix, A. M., Franklin, J. L., Higginbotham, J. N., Zhang, Q., Zimmerman, L. J., Liebler, D. C., Ping, J., Liu, Q., Evans, R., Fissell, W. H., Patton, J. G., Rome, L. H., Burnette, D. T., & Coffey, R. J. (2019). Reassessment of exosome composition. *Cell*, *177*(2), 428–445. e18. <https://doi.org/10.1016/j.cell.2019.02.029>
- Jin, Y., Tan, Y., Chen, L., Liu, Y., & Ren, Z. (2018). Reactive oxygen species induces lipid droplet accumulation in HepG2 cells by increasing perilipin 2 expression. *International Journal of Molecular Sciences*, *19*(11), 3445. <https://doi.org/10.3390/ijms19113445>
- Kalluri, R., & LeBleu, V. S. (2020). The biology, function, and biomedical applications of exosomes. *Science (New York, N.Y.)*, *367*(6478), eaau6977. <https://doi.org/10.1126/science.aau6977>
- Keerthikumar, S., Gangoda, L., Liem, M., Fonseka, P., Atukorala, I., Ozcitti, C., Mechler, A., Adda, C. G., Ang, C.-S., & Mathivanan, S. (2015). Proteogenomic analysis reveals exosomes are more oncogenic than ectosomes. *Oncotarget*, *6*(17), 15375–15396. <https://doi.org/10.18632/oncotarget.3801>
- Laubach, K., Zhang, J., & Chen, X. (2021). The p53 family: A role in lipid and iron metabolism. *Frontiers in Cell and Developmental Biology*, *9*, 715974. <https://doi.org/10.3389/fcell.2021.715974>
- Lazar, I., Clement, E., Dauvillier, S., Milhas, D., Ducoux-Petit, M., LeGonidec, S., Moro, C., Soldan, V., Dalle, S., Balor, S., Golzio, M., Burlet-Schiltz, O., Valet, P., Muller, C., & Nieto, L. (2016). Adipocyte exosomes promote melanoma aggressiveness through fatty acid oxidation: A novel mechanism linking obesity and cancer. *Cancer Research*, *76*(14), 4051–4057. <https://doi.org/10.1158/0008-5472.CAN-16-0651>
- Lehmann, B. D., Paine, M. S., Brooks, A. M., McCubrey, J. A., Renegar, R. H., Wang, R., & Terrian, D. M. (2008). Senescence-associated exosome release from human prostate cancer cells. *Cancer Research*, *68*(19), 7864–7871. <https://doi.org/10.1158/0008-5472.CAN-07-6538>
- Lengyel, E., Makowski, L., DiGiovanni, J., & Kolonin, M. G. (2018). Cancer as a matter of fat: The crosstalk between adipose tissue and tumors. *Trends in cancer*, *4*, 374.
- Li, C., Luo, X., Zhao, S., Siu, G. K., Liang, Y., Chan, H. C., Satoh, A., & Yu, S. S. (2017). COPI – TRAPP II activates Rab18 and regulates its lipid droplet association. *The EMBO Journal*, *36*, 441–457.
- Li, H., Handsaker, B., Wysoker, A., Fennell, T., Ruan, J., Homer, N., Marth, G., Abecasis, G., & Durbin, R., & 1000 Genome Project Data Processing Subgroup. (2009). The sequence alignment/map format and SAMtools. *Bioinformatics (Oxford, England)*, *25*(16), 2078–2079. <https://doi.org/10.1093/bioinformatics/btp352>
- Liu, P., Bartz, R., Zehmer, J. K., Ying, Y. S., Zhu, M., Serrero, G., & Anderson, R. G. (2007). Rab-regulated interaction of early endosomes with lipid droplets. *Biochimica Et Biophysica Acta*, *1773*(6), 784–793. <https://doi.org/10.1016/j.bbamcr.2007.02.004>
- Logozzi, M., Mizzone, D., Angelini, D. F., Di Raimo, R., Falchi, M., Battistini, L., & Fais, S. (2018). Microenvironmental pH and exosome levels interplay in human cancer cell lines of different histotypes. *Cancers*, *10*(10), 370. <https://doi.org/10.3390/cancers10100370>
- Love, M. I., Huber, W., & Anders, S. (2014). Moderated estimation of fold change and dispersion for RNA-seq data with DESeq2. *Genome Biology*, *15*(12), 550. <https://doi.org/10.1186/s13059-014-0550-8>
- Lu, B., Gong, Y., Huang, H., Tang, D., Chen, X., & Kang, R. (2021). Ferroptosis by Lipid Peroxidation: The Tip of the Iceberg? *Frontiers in Cell and Developmental Biology*, *9*, 646890.
- Mathieu, M., Névo, N., Jouve, M., Valenzuela, J. I., Maurin, M., Verweij, F. J., Palmulli, R., Lankar, D., Dingli, F., Loew, D., Rubinstein, E., Boncompain, G., Perez, E., & Théry, C. (2021). Specificities of exosome versus small ectosome secretion revealed by live intracellular tracking of CD63 and CD9. <https://doi.org/10.1038/s41467-021-24384-2>
- Mathieu, M., Martin-Jaular, L., Lavieu, G., & Théry, C. (2019). Specificities of secretion and uptake of exosomes and other extracellular vesicles for cell-to-cell communication. *Nature Cell Biology*, *21*(1), 9–17. <https://doi.org/10.1038/s41556-018-0250-9>
- Muñiz-García, A., Romero, M., Falcón-Perez, J. M., Murray, P., Zorzano, A., & Mora, S. (2022). Hypoxia-induced HIF1 $\alpha$  activation regulates small extracellular vesicle release in human embryonic kidney cells. *Scientific Reports*, *12*(1), 1443. <https://doi.org/10.1038/s41598-022-05161-7>
- Mutschelknaus, L., Azimzadeh, O., Heider, T., Winkler, K., Vetter, M., Kell, R., Tapio, S., Merl-Pham, J., Huber, S. M., Edalat, L., Radulović, V., Anastasov, N., Atkinson, M. J., & Moertl, S. (2017). Radiation alters the cargo of exosomes released from squamous head and neck cancer cells to promote migration of recipient cells OPEN. <https://doi.org/10.1038/s41598-017-12403-6>
- Mylonis, I., Simos, G., & Paraskeva, E. (2019). Hypoxia-inducible factors and the regulation of lipid metabolism. *Cells*, *8*(3), 214. <https://doi.org/10.3390/cells8030214>
- Nisticò, C., Pagliari, F., Chiarella, E., Fernandes Guerreiro, J., Marafioti, M. G., Aversa, I., Genard, G., Hanley, R., Garcia-Calderón, D., Bond, H. M., Mesuraca, M., Tirinato, L., Spadea, M. F., & Seco, J. C. (2021). Lipid droplet biosynthesis impairment through DGAT2 inhibition sensitizes MCF7 breast cancer cells to radiation. *International Journal of Molecular Sciences*, *22*(18), 10102. <https://doi.org/10.3390/ijms221810102>
- Olzmann, J. A., & Carvalho, P. (2019). Dynamics and functions of lipid droplets. *Nature Reviews. Molecular Cell Biology*, *20*(3), 137–155. <https://doi.org/10.1038/s41580-018-0085-z>
- Patro, R., Duggal, G., Love, M. I., Irizarry, R. A., & Kingsford, C. (2017). Salmon provides fast and bias-aware quantification of transcript expression. *Nature Methods*, *14*(4), 417–419. <https://doi.org/10.1038/nmeth.4197>
- Poggio, M., Hu, T., Pai, C. C., Chu, B., Belair, C. D., Chang, A., Montabana, E., Lang, U. E., Fu, Q., Fong, L., & Blleloch, R. (2019). Suppression of exosomal PD-L1 induces systemic anti-tumor immunity and memory. *Cell*, *177*(2), 414–427. e13. <https://doi.org/10.1016/j.cell.2019.02.016>
- Sołtysik, K., Ohsaki, Y., Tatematsu, T., Cheng, J., & Fujimoto, T. (2019). Nuclear lipid droplets derive from a lipoprotein precursor and regulate phosphatidylcholine synthesis. *Nature Communications*, *10*(1), 473. <https://doi.org/10.1038/s41467-019-08411-x>
- Soneson, C., Love, M. I., & Robinson, M. D. (2015). Differential analyses for RNA-seq: Transcript-level estimates improve gene-level inferences. *Fl1000Research*, *4*, 1521. <https://doi.org/10.12688/fl1000research.7563.2>
- Song, J., Mizrak, A., Lee, C. W., Cicconet, M., Lai, Z. W., Tang, W. C., Lu, C. H., Mohr, S. E., Farese, R. V., Jr, & Walther, T. C. (2022). Identification of two pathways mediating protein targeting from ER to lipid droplets. *Nature Cell Biology*, *24*(9), 1364–1377. <https://doi.org/10.1038/s41556-022-00974-0>
- Takasugi, M. (2018). Emerging roles of extracellular vesicles in cellular senescence and aging. *Aging Cell*, *17*(2), e12734. <https://doi.org/10.1111/acer.12734>
- Tang, D., Chen, X., Kang, R., & Kroemer, G. (2021). Ferroptosis: molecular mechanisms and health implications. *Cell Research*, *31*, 107–125.
- Thomou, T., Mori, M. A., Dreyfuss, J. M., Konishi, M., Sakaguchi, M., Wolfrum, C., Rao, T. N., Winnay, J. N., Garcia-Martin, R., Grinspoon, S. K., Gorden, P., & Kahn, C. R. (2017). Adipose-derived circulating miRNAs regulate gene expression in other tissues. *Nature*, *542*(7642), 450–455. <https://doi.org/10.1038/nature21365>
- Tirinato, L., Liberale, C., Di Franco, S., Candeloro, P., Benfante, A., La Rocca, R., Potze, L., Marotta, R., Ruffilli, R., Rajamanickam, V. P., Malerba, M., De Angelis, F., Falqui, A., Carbone, E., Todaro, M., Medema, J. P., Stassi, G., & Di Fabrizio, E. (2015). Lipid droplets: A new player in colorectal cancer stem cells unveiled by spectroscopic imaging. *Stem Cells (Dayton, Ohio)*, *33*(1), 35–44. <https://doi.org/10.1002/stem.1837>
- Tirinato, L., Marafioti, M. G., Pagliari, F., Jansen, J., Aversa, I., Hanley, R., Nisticò, C., Garcia-Calderón, D., Genard, G., Guerreiro, J. F., Costanzo, F. S., & Seco, J. (2021). Lipid droplets and ferritin heavy chain: A devilish liaison in human cancer cell radioresistance. *Elife*, *10*, e72943. <https://doi.org/10.7554/eLife.72943>

- Tirinato, L., Pagliari, F., Di Franco, S., Sogne, E., Marafioti, M. G., Jansen, J., Falqui, A., Todaro, M., Candeloro, P., Liberale, C., Seco, J., Stassi, G., & Di Fabrizio, E. (2019). ROS and lipid droplet accumulation induced by high glucose exposure in healthy colon and Colorectal cancer stem cells. *Genes & Diseases*, 7(4), 620–635. <https://doi.org/10.1016/j.gendis.2019.09.010>
- Tirinato, L., Pagliari, F., Limongi, T., Marini, M., Falqui, A., Seco, J., Candeloro, P., Liberale, C., & Di Fabrizio, E. (2017). An overview of lipid droplets in cancer and cancer stem cells. *Stem Cells International*, 2017, 1656053. <https://doi.org/10.1155/2017/1656053>
- Todaro, M., Gaggianesi, M., Catalano, V., Benfante, A., Iovino, F., Biffoni, M., Apuzzo, T., Sperduti, I., Volpe, S., Cocorullo, G., Gulotta, G., Dieli, F., De Maria, R., & Stassi, G. (2014). CD44v6 is a marker of constitutive and reprogrammed cancer stem cells driving colon cancer metastasis. *Cell Stem Cell*, 14(3), 342–356. <https://doi.org/10.1016/j.stem.2014.01.009>
- Venturella, M., Criscuoli, M., Carraro, F., Naldini, A., & Zocco, D. (2021). Interplay between hypoxia and extracellular vesicles in cancer and inflammation. *Biology*, 10(7), 606. <https://doi.org/10.3390/biology10070606>
- Wells, S. I., Aronow, B. J., Wise, T. M., Williams, S. S., Couget, J. A., & Howley, P. M. (2003). Transcriptome signature of irreversible senescence in human papillomavirus-positive cervical cancer cells. *Proceedings of the National Academy of Sciences of the United States of America*, 100(12), 7093–7098. <https://doi.org/10.1073/pnas.1232309100>
- Xi, L., Peng, M., Liu, S., Liu, Y., Wan, X., Hou, Y., Qin, Y., Yang, L., Chen, S., Zeng, H., Teng, Y., Cui, X., & Liu, M. (2021). Hypoxia-stimulated ATM activation regulates autophagy-associated exosome release from cancer-associated fibroblasts to promote cancer cell invasion. *Journal of Extracellular Vesicles*, 10(11), e12146. <https://doi.org/10.1002/jev2.12146>
- Xu, D., Li, Y., Wu, L., Li, Y., Zhao, D., Yu, J., Huang, T., Ferguson, C., Parton, R. G., Yang, H., & Li, P. (2018). Rab18 promotes lipid droplet (LD) growth by tethering the ER to LDs through SNARE and NRZ interactions. *Journal of Cell Biology*, 217, 975–995.
- Yanatori, I., Richardson, D. R., Dhekne, H. S., Toyokuni, S., & Kishi, F. (2021). “CD63 is regulated by iron via the IRE-IRP system and is important for ferritin secretion by extracellular vesicles”. <https://doi.org/10.1182/blood.2019000962>
- Yáñez-Mó, M., Siljander, P. R., Andreu, Z., Zavec, A. B., Borràs, F. E., Buzas, E. I., Buzas, K., Casal, E., Cappello, F., Carvalho, J., Colás, E., Cordeiro-da Silva, A., Fais, S., Falcon-Perez, J. M., Ghobrial, I. M., Giebel, B., Gimona, M., Graner, M., Gursel, I., ... De Wever, O. (2015). Biological properties of extracellular vesicles and their physiological functions. *Journal of Extracellular Vesicles*, 4, 27066. <https://doi.org/10.3402/jev.v4.27066>
- Yu, X., Harris, S. L., & Levine, A. J. (2006). The regulation of exosome secretion: A novel function of the p53 protein. *Cancer Research*, 66(9), 4795–4801. <https://doi.org/10.1158/0008-5472.CAN-05-4579>
- Yu, X., Riley, T., & Levine, A. J. (2009). The regulation of the endosomal compartment by p53 the tumor suppressor gene. *The FEBS Journal*, 276(8), 2201–2212. <https://doi.org/10.1111/j.1742-4658.2009.06949.x>
- Yue, S., Li, J., Lee, S. Y., Lee, H. J., Shao, T., Song, B., Cheng, L., Masterson, T. A., Liu, X., Ratliff, T. L., & Cheng, J. X. (2014). Cholesteryl ester accumulation induced by PTEN loss and PI3K/AKT activation underlies human prostate cancer aggressiveness. *Cell Metabolism*, 19(3), 393–406. <https://doi.org/10.1016/j.cmet.2014.01.019>
- Zhu, Q. J., Zhu, M., Xu, X. X., Meng, X. M., & Wu, Y. G. (2019). Exosomes from high glucose-treated macrophages activate glomerular mesangial cells via TGF- $\beta$ 1/Smad3 pathway *in vivo* and *in vitro*. *FASEB Journal: Official Publication of the Federation of American Societies for Experimental Biology*, 33(8), 9279–9290. <https://doi.org/10.1096/fj.201802427RRR>

## SUPPORTING INFORMATION

Additional supporting information can be found online in the Supporting Information section at the end of this article.

**How to cite this article:** Genard, G. C., Tirinato, L., Pagliari, F., Da Silva, J., Giammona, A., Alquraish, F., Reyes, M. P., Bordas, M., Marafioti, M. G., Franco, S. D., Janssen, J., Garcia-Calderón, D., Hanley, R., Nistico, C., Fukasawa, Y., Müller, T., Krijgsveld, J., Todaro, M., Costanzo, F. S., ... Seco, J. (2024). Lipid droplets and small extracellular vesicles: More than two independent entities. *Journal of Extracellular Biology*, 3, e162. <https://doi.org/10.1002/jex2.162>